


## TCF periodogram's high sensitivity: A method for optimizing detection of small transiting planets

YASH GONDHALEKAR <sup>1</sup>, ERIC D. FEIGELSON <sup>2,3,4</sup>, GABRIEL A. CACERES,<sup>5</sup> MARCO MONTALTO,<sup>6</sup> AND SNEHANSHU SAHA<sup>1</sup>

<sup>1</sup>*Birla Institute of Technology and Science, Pilani, Goa, India*

<sup>2</sup>*Department of Astronomy & Astrophysics, Pennsylvania State University, 525 Davey Laboratory, University Park, PA 16802, USA*

<sup>3</sup>*Center for Astrostatistics, Pennsylvania State University, 525 Davey Laboratory, University Park PA, 16802, USA*

<sup>4</sup>*Center for Exoplanets and Habitable Worlds, Pennsylvania State University, 525 Davey Laboratory, University Park PA, 16802, USA*

<sup>5</sup>*EY-Parthenon, 1540 Broadway, New York NY, 10036, USA*

<sup>6</sup>*INAF - Osservatorio Astrofisico di Catania, Via S. Sofia 78, I-95123 Catania, Italy*

(Received Version July 31 2023)

### ABSTRACT

We conduct a methodological study for statistically comparing the sensitivities of two periodograms for weak signal planet detection in transit surveys: the widely used Box-Least Squares (BLS) algorithm following light curve detrending and the Transit Comb Filter (TCF) algorithm following autoregressive ARIMA modeling. Small depth transits are injected into light curves with different simulated noise characteristics. Two measures of spectral peak significance are examined: the periodogram signal-to-noise ratio (SNR) and a False Alarm Probability (FAP) based on the generalized extreme value distribution. The relative performance of the BLS and TCF algorithms for small planet detection is examined for a range of light curve characteristics, including orbital period, transit duration, depth, number of transits, and type of noise. The TCF periodogram applied to ARIMA fit residuals with the SNR detection metric is preferred when short-memory autocorrelation is present in the detrended light curve and even when the light curve noise had white Gaussian noise. BLS is more sensitive to small planets only under limited circumstances with the FAP metric. BLS periodogram characteristics are inferior when autocorrelated noise is present. Application of these methods to TESS light curves with small exoplanets confirms our simulation results. The study ends with a decision tree that advises transit survey scientists on procedures to detect small planets most efficiently. The use of ARIMA detrending and TCF periodograms can significantly improve the sensitivity of any transit survey with regularly spaced cadence.

*Keywords:* Period search (1955), Time series analysis (1916), Transits (1711), Exoplanet detection methods (489), Transit photometry (1709)

### 1. INTRODUCTION

#### 1.1. Difficulties with detecting small transiting planets

The transits of giant Jovian planets producing periodic  $\sim 1\%$  dips in brightness can be easily seen in light curves from photometric light curves produced by space-based observatories such as COROT (Baglin et al. 2008), Kepler (Borucki et al. 2010), K2 (Howell et al. 2014), TESS (Ricker et al. 2015), and the forthcoming PLATO (Rauer et al. 2014) and Roman Space Tele-

scope (Spergel et al. 2015) missions. However, achieving planned goals to discover suspected large populations of smaller planets has proved challenging. Predictions that several thousand transiting planets will emerge from analysis of TESS data (Barclay et al. 2018; Kunimoto et al. 2022) are, at present, overly optimistic<sup>1</sup>. Problems arise because transits from smaller rocky planets producing 0.01% – 0.1% periodic photometric dips

<sup>1</sup> A similar discrepancy between predicted and achieved transiting samples was noted by Horne (2003) from early ground-based transit surveys.

are often masked by other sources of photometric variability (Gilliland et al. 2011): rotational modulation of starspots (McQuillan et al. 2014); microvariability from stochastic stellar magnetic activity (Aigrain et al. 2004); contamination by eclipsing binaries blended in the large pixels of wide-field telescopes (Torres et al. 2011); instrumental effects involving satellite operations (Vanderburg & Johnson 2014); red noise (Pont et al. 2006) and unavoidable detector photon noise.

The challenge of small planet detection requires solving complicated problems in time series analysis. Several stages of analysis are needed:

1. The light curve is detrended to remove aperiodic or quasi-periodic variations unrelated to strictly periodic planetary orbits. Detrending is typically pursued using nonparametric or semi-parametric methods such as spline fitting, wavelet transforms, or Gaussian Processes regression (e.g. Jenkins et al. 2002; Lightkurve Collaboration et al. 2018a; Feinstein et al. 2019; Montalto et al. 2020; Foreman-Mackey et al. 2021; Guerrero et al. 2021).
2. The detrended light curve is typically searched for transit-shaped periodic dips using the parametric Box-Least Squares (BLS) algorithm developed by Kovács et al. (2002). For each trial period, a box-shaped signal is fit to the folded light curve for a range of transit durations and phases. A BLS periodogram is constructed of the most profound signal found at each period, and spectral peaks are investigated as possible transit signals. Kovács et al. (2002) show that this procedure is more sensitive to faint box-shaped dips than Fourier periodograms (or, for irregular observation cadences, Lomb-Scargle periodograms Scargle 1982) that search for sinusoidal signals or non-parametric periodograms that search for arbitrarily shaped signals such as phase dispersion minimization (Stellingwerf 1978).
3. Procedures are applied to cull False Alarms and False Positives (particularly contaminant eclipsing binaries) from spectral peaks above some threshold. This typically involves a combination of machine learning classification (such as Random Forest or neural network) and human or automated vetting. Vetting procedures for transit planet detection are discussed by Thompson et al. (2015), Twicken et al. (2018), Hedges (2021), Guerrero et al. (2021), Melton et al. (2023a) and others.

For the Kepler and TESS space missions, these procedures are used by NASA science teams to generate Ke-

pler and TESS Objects of Interest (KOIs and TOIs) that are then passed to ground-based telescopes for further study (Twicken et al. 2016; Guerrero et al. 2021).

However, these standard procedures for planet detection may have technical deficiencies that other statistical approaches might improve. At least two issues might be considered. First, detrenders based on a function with a kernel or a mother wavelet with bandwidth can miss short-memory variations. The main concern is stochastic autoregressive variations characteristic of stellar magnetic activity. Its presence can be easily checked by plotting the autocorrelation function of the detrended light curve to see if short-memory autoregressive behaviors are present. Formal statistical time series diagnostics, such as the Shapiro-Wilk and Ljung-Box tests, can determine if the light curves deviate from Gaussian white noise. This is a non-trivial situation: 36% of light curves from TESS Full Frame Images (FFIs) show statistically significant short-memory stochastic variability after spline detrending (Melton et al. 2023b, their Figure 5).

Second, periodograms have complicated and poorly understood statistical properties that hinder the straightforward identification of significant peaks representing actual periodic behaviors. Even in classical Fourier analysis, the theorems underlying the statistical distribution of periodogram peaks apply only to the unrealistic situation of an infinitely long, uninterrupted, evenly-spaced data stream of Gaussian white noise with a single sinusoidal signal (Percival & Walden 2009). Spurious spectral peaks can arise from periodic instrumental effects (such as data gaps associated with the satellite orbital period or data downloads) for realistic time series arising from space-based missions. Complicated aliases of true signals often appear (VanderPlas 2018). Periodograms can exhibit undesirable behaviors even when no interesting signal is present: Ofir (2014) shows that the noise properties of BLS periodograms often have trends in value and noise (heteroscedasticity) as a function of the trial period.

The first issue concerning autoregressive variations that may escape removal by detrenders has a clear treatment using low-dimensional parametric autoregressive moving average (ARMA) models. These are commonly combined with a simple nonparametric detrender involving ‘differencing’ (or differentiating) the time series. The resulting ARIMA modeling (also known as Box-Jenkins analysis) and its many extensions have dominated analyses of stochastic time series for the past 50 years in engineering signal processing, econometrics, and other fields. Autoregressive modeling dominates most textbooks; the foundational text by Box et al. (2015) has

over 50 thousand citations, and a Nobel Prize in Economics was awarded for the non-linear GARCH model that introduced stochastic volatility to the simpler linear ARIMA model.

ARIMA detrending for transiting planet detection was introduced by [Caceres et al. \(2019a\)](#) and found to be effective in reducing unwanted light curve variations in most Kepler and TESS light curves ([Caceres et al. 2019b](#); [Melton et al. 2023b](#)). The utility of ARMA-type modeling for astronomical time domain studies is, in general, discussed by [Feigelson et al. \(2018\)](#).

However, the traditional BLS algorithm can not be used on ARIMA residuals because the differencing operation changes a sequence of box-shaped into a sequence of double spikes. [Caceres et al. \(2019a\)](#) developed the Transit Comb Filter<sup>2</sup> (TCF) as an alternative algorithm to produce periodograms of ARIMA residuals. As the double spike reflect only the ingress and egress, it would seem to have less information and therefore be less sensitive to weak transits than BLS fitting. However, in searching for small planets in the 4-year Kepler data, [Caceres et al. \(2019b\)](#) find that the TCF periodogram has low noise and is remarkably sensitive to faint transits corresponding to Earth- and Mars-sized planets. Similarly, [Melton et al. \(2023c\)](#), their Figure 16) find that the ARIMA-TCF procedure tends to find smaller planets than other pipelines used to generate TOIs.

In addition to the choice of the periodogram algorithm, the transit scientist must decide on the best measure for the strength of a spectral peak. The most straightforward approach is to locate the period with the highest periodogram power. However, strong peaks can be due to autocorrelated noise in the light curve or aliasing associated with an irregular cadence. Noting heteroscedasticity and trends in periodograms' response to noise, [Ofir \(2014\)](#) recommends using local signal-to-noise ratios of the detrended BLS periodogram.

Evaluating False Alarm Probabilities (FAPs) associated with the chosen measure is also tricky. This has been extensively discussed in the context of Lomb-Scargle periodograms. Early analytic FAPs for LSPs ([Scargle 1982](#); [Horne & Baliunas 1986](#)) were shown to be unreliable (e.g., [Koen 1990](#)), and numerous improvements were suggested. One outcome of these astrostatistical analyses is that procedures that ignore most periodogram noise values might better measure true periodicities. The statistical field of extreme value theory (EVT) based on the Fisher-Tippett-Gnedenko Theorem

provides a mathematical foundation for evaluating peak significance in astronomical LSPs ([Baluev 2008](#)).

EVT has been widely applied to problems in geology, finance, and engineering; for example, EVT helps evaluate whether a storm exceeds a '100-year hurricane' or whether a sudden stock market change is a fluctuation or a 'crash'. The mathematics and many applications of EVT appear in texts like [Coles et al. \(2001\)](#) and [Castillo et al. \(2004\)](#). The application of EVT to periodogram FAPs has been discussed in astrostatistical studies ([Baluev 2008](#); [Süveges 2014](#); [Süveges et al. 2015](#); [Sulis et al. 2017](#); [Vio et al. 2019](#); [Delisle et al. 2020](#); [Koen 2021](#); [Giertych et al. 2022](#)) and the review by [VanderPlas \(2018\)](#). EVT is also gaining increased attention in astronomical applications, including solar, stellar, galaxy, and cosmological studies (e.g. [Asensio Ramos 2007](#); [Pratt et al. 2017](#); [Waizmann et al. 2012](#); [Davis et al. 2011](#)). We are guided by the approach of [Süveges \(2014\)](#) for our application to transiting planet periodograms.

## 1.2. Scope of This Study

The present study aims to investigate statistical issues related to the behaviors of BLS and TCF periodograms and their sensitivities to small planetary transit signals under different noise conditions. As it may be less familiar to astronomers, we provide a background on extreme value theory and its application to periodogram peak significance in §2. Much of our effort is based on the analysis of simulated light curves described in §3.1, where we discuss two metrics to evaluate the significance of periodogram peaks. This reveals previous properties of the two periodograms that extend the work of [Ofir \(2014\)](#) and show their dependencies on light curve properties (§4-5). We then illustrate the two periodograms on real TESS light curves with known small planets (§6). After a discussion of the findings (§7), the study ends with advice to transit survey scientists on the best approaches for small planet detection (§8).

Our analysis is not intended to be a comprehensive study of periodograms for transit study. The effort here is limited to comparing the performance of two periodograms, BLS and TCF, applied to light curves with continuous evenly-spaced cadences. Both are low-dimensional parametric procedures with fixed functional forms at a chosen trial period: a rectangular box for BLS and a double-spike pattern for TCF.

We do not consider other periodograms based on sinusoidal variations, such as the Schuster periodogram of classical Fourier analysis or its Lomb-Scargle extension to irregular observing cadences ([Scargle 1982](#)), nor do we consider nonparametric periodograms such as phase

<sup>2</sup> The TCF can be considered an extension of the Dirac comb or Shah function used in engineering signal processing.

dispersion minimization (Stellingwerf 1978) and minimum string length (Dworetsky 1983). The Transit Least Squares (TLS) algorithm (Hippke & Heller 2019), an important variant of BLS with ingress and egress transit shapes arising from astrophysical modeling, is not analyzed. Period search procedures with different statistical approaches are not treated, including Waldmann (2012) and Zucker (2015). We also ignore evaluations of periodicity significance in the time domain, such as the classical Wald test (Pont et al. 2006). We assume datasets with evenly spaced time series (although missing data may exist). Thus, we do not consider highly irregular light curves typically emerging from ground-based telescopic surveys. Our calculations use the original BLS algorithm of Kovács et al. (2002), and we only briefly mention faster algorithms in Appendix A. Comparison of period finding algorithms, although with different focuses, have been studied in previous studies (e.g., Graham et al. 2013 and references therein).

One method not examined here may have high sensitivity to small planets. Gregory & Loredó (1992) formulate a likelihood for Bayesian period search assuming an arbitrarily shaped transit. A sensitive likelihood-based periodogram might emerge if one inserts a strong prior for a box-shaped variation with a small duty cycle.

## 2. PERIODOGRAMS AND EXTREME VALUE THEORY

Periodograms are a common way to search for periodicities in astronomical time series. They evaluate the value of a test statistic at all independent periods or frequencies (VanderPlas 2018; Giertych et al. 2022). A candidate periodicity corresponds to a period where a measure of periodogram power is maximum and lies well above the periodogram noise.

Evaluating the statistical and scientific significance of a trial periodicity is tricky. Periodogram power values may not follow a well-defined distribution, they may exhibit trends and heteroscedasticity with the period, and strong spurious (False Alarms) (Brown 2003) or alias peaks may be present (Frescura et al. 2008; Ofir 2014; VanderPlas 2018). A commonly used quantity to characterize the significance of the peak of a periodogram is the False-alarm Probability (FAP), the probability that the maximum value of the periodogram or higher is observed under the null hypothesis  $H_0$  that the observed time series does not contain a periodic component. The alternative hypothesis  $H_1$  is that a deterministic periodic signal is present. Typically, one chooses a significance level, such as  $\alpha = 0.01$ , and declares the peak significant, hence claiming detection of a transiting planet if  $\text{FAP} < \alpha$ .

A straightforward attempt to estimate the distribution of maximum<sup>3</sup>  $M_n = \max\{X_1, X_2, \dots, X_n\}$ , where  $X_1, X_2, \dots, X_n$  are independent and identically distributed (i.i.d) random variables, is

$$\begin{aligned} P(M_n \leq z) &= P(X_1 \leq z, X_2 \leq z, \dots, X_n \leq z) \\ &= P(X_1 \leq z) \times P(X_2 \leq z) \cdots \times P(X_n \leq z) \\ &= \{F(z)\}^n \end{aligned} \tag{1}$$

where  $F(z)$  is the cumulative distribution of the periodogram under the null hypothesis. In this case, the FAP can be written as

$$\text{FAP} = 1 - \{F(z)\}^n. \tag{2}$$

However, several difficulties arise in applying this FAP formula from EVT in real applications (see discussion in Süveges 2014):

1. The dependence on the assumption of i.i.d. for the random variable does not apply to periodograms where the same photometric data is used for each trial period. In particular, there is considerable dependence in the folded data for periods related by harmonics with factors of 2 or 3.
2. It is not straightforward to evaluate  $n$ , the number of independent frequencies, due to an irregular cadence or the oversampling of the periodogram needed to capture accurate peak values. This problem is widely discussed (e.g. Horne & Baliunas 1986; Frescura et al. 2007; Frescura et al. 2008; Koen 2010; VanderPlas 2018).
3. The distribution function,  $F(z)$ , is generally unknown or known only approximately. While techniques to estimate  $F$  from the sample exist, small errors in  $F$ 's estimation can cause large errors in  $F(z)^n$ . For example, the small difference between the observed light curve variance and its population variance can produce major errors in FAPs (Koen 1990).
4. Consider the behavior of  $F(z)^n$  when  $n \rightarrow \infty$ : since  $0 \leq F(z) \leq 1$ ,  $F(z)^n \rightarrow 0$  as  $n \rightarrow \infty$ ,  $\forall z < z_+$ , where  $z_+$  is the upper end-point of  $F$  (i.e. the smallest  $z$  such that  $F(z) = 1$ ). This

<sup>3</sup> In some situations, it is not clear whether the extreme value is part of the stochastic process generating most of the data or whether it is a contaminant from another population. Since the periodogram power values are calculated in a consistent fashion from a single dataset, their peak values can not be extraneous contaminants and can be legitimately evaluated using extreme value theory.

means that the distribution of  $F(z)^n$  degenerates as  $n$  increases, which is undesirable since stabilization is not guaranteed (Coles et al. 2001).

The application of EVT to the detection of periodicities in astronomical periodograms has focused on the Lomb-Scargle periodogram, the generalization of the Fourier periodogram for irregularly spaced cadences (Baluev 2008; Süveges 2014; Süveges et al. 2015; Sulis et al. 2017; Vio et al. 2019; Delisle et al. 2020; Koen 2021; Giertych et al. 2022). Here we extend the procedure to periodograms specializing in planetary transit detection.

The Fisher–Tippett–Gnedenko theorem (also called the Extreme Value Theorem) lies at the foundation of EVT. It suggests that the maxima of a large sequence of i.i.d. univariate random variables after some standardization (see below) asymptotically follow well-defined distributions (Fisher & Tippett 1928; Gnedenko 1943). The theorem’s assumptions are very general, similar to those of the Central Limit Theorem for the asymptotic behavior of mean values. In both cases, the distribution  $F$  of the variable does not need to be known; the theorem is valid for data drawn from almost all continuous distribution functions.

Consider again the maximum value  $M_n$  of a sequence of  $n$  i.i.d. random variables  $x_1, x_2, \dots, x_n$ . Start by standardizing a sequence of  $n$  real-valued observations  $M_n$  using sequences of constants  $\{a_n > 0\}$  and  $\{b_n\}$  to yield  $M_n^* = \frac{M_n - a_n}{b_n}$ . The Extreme Value Theorem states that, under broad conditions, the limiting distribution of  $M_n^*$ ,  $P(M_n^* \leq x)$ , converges to distribution  $G$  belonging to the Gumbel, Fréchet, or Weibull families. These families are conveniently combined into the Generalized Extreme Value (GEV) distribution (Jenkinson 1955), a three-parameter distribution with parameters  $\mu$ ,  $\sigma$ , and  $\xi$  denoting the location, scale, and shape:

$$\begin{aligned} G(x) &= P(M_n^* \leq x) \\ &= \exp\left\{-\left(1 + \xi \left(\frac{x - \mu}{\sigma}\right)\right)^{-1/\xi}\right\} \end{aligned} \quad (3)$$

where  $1 + \xi \left(\frac{x - \mu}{\sigma}\right) > 0$  and  $\sigma > 0$ ,  $\mu \in \mathbb{R}$ , and  $\xi \in \mathbb{R}$ . If the shape parameter  $\xi = 0$ , then  $1/\xi$  is undefined and the expression reduces to

$$G(x) = \exp\left\{-\exp\left(\frac{x - \mu}{\sigma}\right)\right\} \quad (4)$$

by continuity; this is called the Gumbel distribution. The Fréchet and Weibull families correspond to  $\xi > 0$  and  $\xi < 0$ , respectively. If  $\xi > 0$  and  $\xi \left(\frac{x - \mu}{\sigma}\right) \leq -1$ ,

then  $G(x) = 0$  and if  $\xi < 0$  and  $\xi \left(\frac{x - \mu}{\sigma}\right) \leq -1$ , then  $G(x) = 1$ . If one is interested in minimal rather than maximal values, the corresponding expressions for minima are obtained by replacing  $x$  with  $-x$ . Probabilities for the GEV distributions are calculated with CRAN package `extRemes` (Gilleland & Katz 2016).

Two widely used approaches to evaluate the significance of extrema in EVT are the block-maxima and the peaks-over-threshold methods (Coles et al. 2001). In the block-maxima approach, data is partitioned into blocks of a certain size, and the maximum from each block is used to generate a sample of extreme values on which the GEV model can be fit. The peaks-over-threshold selects extreme value samples by selecting values higher or lower than a chosen threshold, followed by declustering to try to achieve independence. The block-maxima method is a natural choice for periodograms because it accounts for short-range dependences in the periodogram and can be practically easier to use (Ferreira & de Haan 2015).

An advantage of the EVT approach is that  $n$ , the number of independent values in the dataset, does not appear in the GEV distribution, as in equations (1)–(2). However, other difficulties seen with earlier FAP estimates remain. Harmonics of true periodicities with spectral peak strengths comparable to the true period will tend to overpopulate the extreme values and distort GEV probabilities. Heteroscedasticity and trends in the periodogram noise as a function of period violate the i.i.d. assumptions. This can be partially compensated by detrending and standardizing<sup>4</sup> the periodogram; that is, using local signal-to-noise ratios rather than periodogram power directly as advocated by Ofir (2014) and our treatment below (§3.2).

Most importantly, the assumption that the dataset  $x_i$  is i.i.d. (i.e., homoscedastic white noise) will not apply to many astronomical periodograms. This assumption of the extreme value theorem can be relaxed under some circumstances; for example, the theorem is valid for dependent variables provided the dependence decays for increasingly separated variables when  $n \rightarrow \infty$  (Leadbetter & Rootzen 1988). However, this condition is not met for oversampled periodograms.

<sup>4</sup> The usual method of standardization is to subtract the mean and divide by the standard deviation. However, due to the non-Gaussianity of periodogram power values, we advocate a robust standardization that does not depend on normality; see equation (6). Sulis et al. (2017) provide a discussion of standardized periodograms for exoplanet detection from radial velocity observations.

Therefore, treating periodograms under EVT requires a computational approach in place of the asymptotic analytic formulae (3)-(4). The most widely used approach, nonparametric bootstrap resampling, is inadequate due to its assumptions of i.i.d. and the burden of computing periodograms with many trial periods for each bootstrap resample. Süveges (2014) propose a more efficient procedure involving bootstrapping partial periodograms over randomly chosen ranges of periods. This hybrid approach combining extreme value statistics and bootstrap resampling is favorably reviewed by VanderPlas (2018) and Koen (2021) for astronomical periodograms. We adopt this approach here (§3.3).

### 3. SIMULATED LIGHT CURVES

#### 3.1. Construction and Analysis of Simulated Light Curves

Simulations provide an excellent way to assess and compare periodogram peak significance due to the full control over noise conditions. Our simulations are designed to roughly resemble single-sector observations from the TESS satellite prime mission survey. The light curves have a uniform 0.5 hr observing cadence. No gaps in observations are included. The noise behaviors are stationary—no changes during the entire time span of the light curve are modeled. In analogous to observed light curves, this implies that nonstationarity has previously been removed with a detrending procedure: moving average filter, spline or Gaussian Processing regression, wavelet transform, or similar operation.

Two noise models are constructed. The first assumes Gaussian white noise with mean 0 and standard deviation  $\sigma_0 = 1 \times 10^{-4}$  or 100 parts-per-million (ppm). This is characteristic of TESS photon noise levels for bright stars with  $T \simeq 7 - 8$  where super-Earths might be detected around solar mass stars, and is similar to the simulation noise level assumed by Hippke & Heller (2019).

The second noise model assumes an autoregressive moving average (ARMA) process with order ARMA(3,3) and coefficients sufficiently high to give statistically significant autocorrelation up to  $\simeq 5$  hours. Specifically, we assume the flux value  $X_t$  at time  $t$  is

$$X_t = \sum_{i=1}^3 \phi_i X_{t-i} + \sum_{i=1}^3 \theta_i \epsilon_{t-i} + \epsilon_t \quad (5)$$

where  $\epsilon_t = N(0, \sigma^2)$  is a white noise process with  $\sigma = 1 \times 10^{-4}$  and the ARMA coefficients are set to

$\phi = (0.2, 0.3, 0.2)$  and  $\theta = (0.2, 0.2, 0.3)$ <sup>5</sup>. While these coefficients may be larger than realistically present in many detrended TESS light curves, the simulations are designed to reveal clear differences between periodogram performance for white and correlated noise. For reference, ARIMA models have been applied to large samples of Kepler and TESS light curves by Caceres et al. (2019b) and Melton et al. (2023b), respectively, based on the methodology described by Caceres et al. (2019a) and Melton et al. (2023a).

Simulations with a hypothetical transiting planet contain periodic transits with varying characteristics such as the orbital period, transit depth, duration, noise type, and total transits (§5). The shape of the transits is modeled as a trapezoid with 30 min ingress and egress; limb darkening, impact factor, and other possible effects are not included. We simulate only one planet; systems with multiple transiting planets producing multiple periodic light curves are not examined.

Before calculating the BLS periodogram when autoregressive noise is simulated (but not when pure Gaussian noise is simulated), the simulated light curves are subject to Gaussian Processes regression, which removes trends but may leave short-memory autocorrelation. We use the software implementation *gausspr* in CRAN package *kernelab* (Karatzoglou et al. 2023) within the R statistical software environment (R Core Team 2022) based on the methodology described by Karatzoglou et al. (2004) and Williams & Barber (1998). We use the squared exponential kernel (the radial basis kernel function) as the covariance function. The kernel width hyperparameter is set using a heuristic to set a reasonable value based on the data (controlled by the keyword `kpar = 'automatic'`).

Before calculating the TCF periodogram, the simulated light curves are subject to ARIMA modeling that effectively removes both trends and short-memory autocorrelation, leaving residuals close to white noise. We use the software implementation *auto.arima* in CRAN package *forecast* that automatically calculates maximum likelihood fits for a range of (p,0,q) orders and selects the best model based on the Akaike Information Criterion that is penalized for model complexity (Hyndman & Khandakar 2008; Hyndman et al. 2023). We restrict model complexity to  $p, q \leq 5$ .

Periodograms are then calculated from the detrended light curves to reveal transit-shaped periodic behaviors. As outlined in §1, we will be examining the sensitiv-

<sup>5</sup> Note that the ARMA model here is actually a superposition of autoregressive and Gaussian (due to the  $\epsilon$  error term). For notation ease throughout, we have called it autoregressive.

ity of two periodograms – BLS and TCF – and two measures of significance in periodogram peaks: an SNR that takes into account trends and heteroscedasticity in periodogram noise; and an EVT-based probability of a standardized periodogram that ignores periodogram noise and considers only extreme values. Such a combination has been used since both metrics have their advantages and disadvantages: FAPs affected by aliasing—a common feature in astronomical periodograms (Baluev 2013; Baluev 2008; Süveges 2014); SNR affected by complex alias structures, non-Gaussianity (Caceres et al. 2019a). These significance measures are described in §3.2 and §3.3, respectively.

### 3.2. Periodogram Peak Metric Based on Signal-to-Noise Ratios

It is not improbable that a periodicity from a small planet produces a peak in a periodogram that can not be unambiguously interpreted as a transiting planet due to the noise characteristics of the periodogram in surrounding frequencies. If the periodogram power values and noise variance are not stationary (i.e., not homoscedastic), this problem can not be effectively captured in bootstrap procedures as used in EVT-based analysis (§3.3). However, this situation is treated by a local SNR measure providing the noise is estimated using frequencies close to the peak of interest. We emphasize that the noise considered here is in the frequency-domain periodogram, not the noise in the original time-domain light curve as considered in many other studies (e.g. Kovács et al. 2002; Pont et al. 2006; Fressin et al. 2013; Dressing & Charbonneau 2015).

To account for the periodogram trends (typically a rise in the mean level of the periodogram with the increasing period as noted by Ofir 2014), the periodogram is detrended using a smoother designed to be robust against non-Gaussianity and outliers. We use the median (50% quantile) curve of a quadratic smoothing B-splines with roughness penalty parameter  $\lambda = 1$  using the method developed by Ng (1996) and Ng & Maechler (2007). Twenty equally-spaced spline knots are used. Code implementation is provided by CRAN package *cobs* (Ng & Maechler 2022).

We then define the SNR of the periodogram peak as

$$\text{SNR} = \text{Power}_{\text{peak}}/\text{MAD}_{\text{peak}} \quad (6)$$

where  $\text{Power}_{\text{peak}}$  denotes the peak periodogram power,  $\text{MAD}_{\text{peak}}$  is the median absolute deviation of nearby periodogram powers measured in a window of frequencies around the peak under study after the periodogram has been detrended (§3.1).

The MAD is a robust measure of local scatter that, unlike the usual root-mean-square  $\sigma$  value, is insensi-

tive to strong non-Gaussianity of periodogram noise values. The MAD is used in this context, for example, by Vanderburg et al. (2016) in a search for K2 transiting planets. However, there is little guidance on defining a ‘nearby’ region of the periodogram to measure the noise; we select a window of 3000 periods symmetrically centered around the peak. This choice is generally sufficiently large to give a good estimate of the MAD but sufficiently narrow to avoid heteroscedasticity (changes of noise amplitude with the period) in the periodogram.

### 3.3. Periodogram Peak Metric Based on EVT False Alarm Probabilities

Our approach for applying EVT (§2) to periodogram peak evaluation closely follows Süveges (2014); see also Suveges (2012) and Süveges et al. (2015). Here a non-parametric bootstrap procedure is combined with EVT to estimate FAPs for the peak in a periodogram. The first step is generating  $R$  bootstrap samples from the original time series. The next step is calculating the periodogram for each of the  $R$  bootstrapped series and selecting the maximum of each periodogram, where each periodogram is computed on  $K \times L$  frequencies selected from the entire frequency grid. This yields a sample of  $R$  maximum values to which the GEV distribution is fit to obtain the FAP of the peak in the original periodogram. These  $K \times L$  frequencies are selected by randomly selecting  $L$  non-overlapping frequency intervals, each with  $K$  consecutive frequencies. Such a selection ensures that long-range dependencies are accounted for due to  $L$ , while short-range dependencies (spectral leakage) are accounted for due to  $K$ .

We have conducted tests to ensure that the sensitivity to faint planets evaluated using our EVT procedures is largely independent of reasonable choices of  $R$  (100 – 500),  $K$  (1 – 5), and  $L$  (100 – 500), similar to the stability experiments performed by Süveges (2014). These tests were made for simulated light curves with Gaussian and autoregressive noise. One might also predict that unnecessarily higher oversampling might introduce spurious small-scale structures in the periodogram. This effect might be present for  $K \simeq 10 - 20$  but is not seen in our simulations for  $K \leq 5$ .

A GEV distribution is then fit by maximum likelihood to the sample of  $R$  maxima to obtain the FAP of the peak in the original periodogram. The quality of the GEV fit is checked with the Anderson-Darling test (Stephens 1974), requiring  $p$ -value  $> 0.01$ . A similar ‘shortcut’ described in Koen (2015) was used: the three estimated GEV parameters were treated as known while calculating the  $p$ -value for these tests. This goodness-of-fit test is needed because the GEV is only a limiting

distribution. If the model is deemed valid, it can be used for estimating the FAP of the observed peak in the periodogram. Here

$$\text{FAP} = 1 - \widehat{G}(x) \quad (7)$$

where  $\widehat{G}$  is the fitted GEV distribution, and  $x$  is the peak power of the periodogram calculated on the original time series. Despite the common practice of oversampling periodograms, which introduces dependency, approaches based on EVT have shown plausible results, provided one has verified the GEV fit quality.

To facilitate the comparison of periodograms using FAPs, we apply the EVT procedure described above on “standardized” periodograms, i.e., with its trend removed and normalized by the local scatter, that converts the periodogram powers to similar scales. The detrending is performed with the same procedure used for SNR calculation described in §3.2. The local scatter of the detrended periodogram is then estimated as a running MAD using ten windows in the entire frequency grid. The periodogram powers at the edge of the frequency grid are handled by taking their MAD. The local scatter implementation is taken from the `runmad` function from the `caTools` CRAN package version 1.17.1. We advocate the use of a “local” scatter measure rather than a “global” scatter measure used previously by, e.g., Hippke & Heller (2019), to account for the heteroscedastic noise structure observed in the BLS and TCF periodograms (Ofir 2014; Caceres et al. 2019a). Standardization is also performed on the partial periodograms before extracting their maxima for GEV fitting.

As discussed in §2, it is important to note that this approach is not directly applicable to correlated time series. However, here the light curves have been detrended prior to periodogram applications when correlated noise is simulated and thus are close to uncorrelated. We remind the reader that detrending is needed twice: once on the light curves and second on the periodograms; however, both differ.

#### 4. DETAILED EXAMINATION OF A SINGLE TRIAL OF TRANSITING PLANETS

We show the results on BLS and TCF periodograms with SNR and FAP peak evaluation metrics for simulated light curves with Gaussian and autoregressive noise characteristics described above. For illustration here, we have injected transit signals for planets with two different sizes assuming an orbital period of two days and a two-hour transit duration. The results are shown in Figures 1-4.

In the simulation with Gaussian noise, the transits can be seen visually in the light curve for the larger

planet (simulated depth = 200 ppm, Figure 1), but they are lost in the noise for the smaller planet (simulated depth = 68 ppm, Figure 2). The signal is recovered for the larger planet and only marginally recovered for the smaller planet by the BLS and TCF periodograms. However, the TCF gives a substantially stronger signal for Gaussian noise: SNR = 40.1 *vs.* 20.8 for the larger planet and 11.1 *vs.* 7.5 for the smaller planet. Upward trends in noise values are seen in the TCF periodogram for longer periods (red *cobs* curves) that are removed by standardization (fourth row). The BLS periodogram shows heteroscedasticity in noise as the period changes, as noted previously by Ofir (2014) and Caceres et al. (2019a). Similar to Ofir (2014), we observe that the BLS scatter increases at longer periods (i.e., smaller frequencies) in the periodogram, which was found by observing an increasing trend in the scatter estimate described in §3.3. Thus, an increasing trend in the power and the power scatter towards longer periods suggests that the distribution of powers at shorter and longer periods could be different.

Although the TCF has greater sensitivity than BLS using the SNR metric due to a higher SNR, BLS is considerably more sensitive using the FAP metric. This is shown in the annotations in the fourth rows of Figures 1-2 where FAP  $\sim 5 \times 10^{-5}$  for BLS and  $\sim 4 \times 10^{-2}$  for TCF with the smaller simulated planet. For the larger planet, secondary peaks are mostly aliases of the injected 2.0 day period, while random noise peaks are the principal source of secondary peaks for the smaller planets.

Figures 3-4 show the periodogram analysis using autoregressive noise. It is difficult to unambiguously see the 2-day transits visually in the light curve, even for a planet with depth = 400 ppm, twice the depth needed for a similar SNR for TCF when only Gaussian noise was present. With autoregressive noise, the ARIMA fitting and the TCF periodogram give SNR = 44.1, while the BLS periodogram is severely degraded with SNR = 8.2. Here a strong trend in BLS periodogram power levels for periods without true signal is present. Standardization of the BLS periodogram removes this strong trend (fourth row of Figure 3). However, the FAP value of  $4 \times 10^{-4}$  is now worse than for the TCF periodogram, where standardization is not essential.

The situation for the smaller planet in the presence of autoregressive noise is similar to the larger planet (Figure 4). The TCF periodogram captures the injected periodic transit without difficulty (SNR = 21.6), while it is hardly detected in the BLS periodogram (SNR = 4.3). The FAP metric gives a significant detection for TCF (FAP =  $7 \times 10^{-7}$ ) but only a marginal detection for

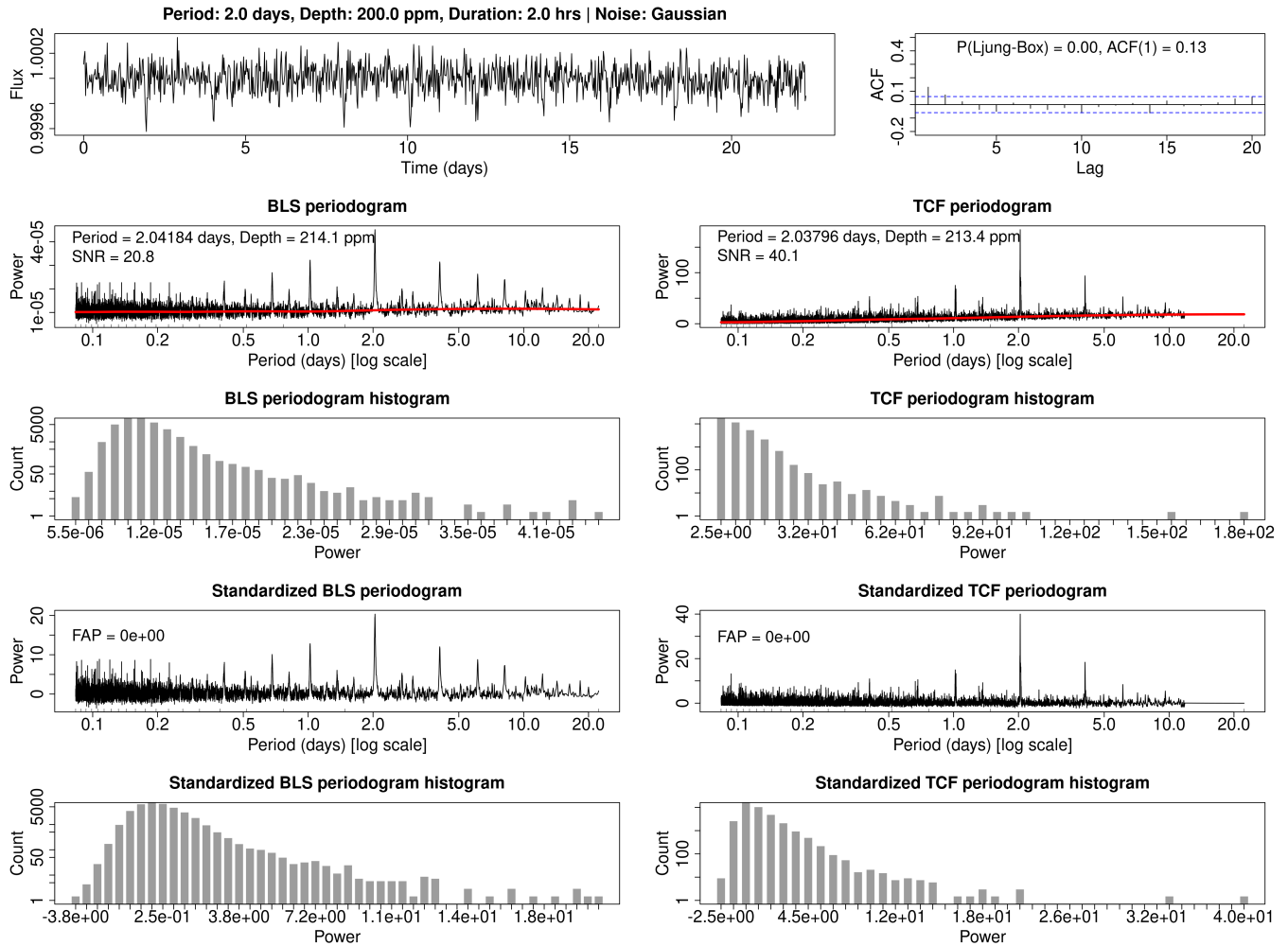


**Figure 1.** Periodogram analysis of a simulated light curve with Gaussian white noise together with an injected planetary transit with depth 200 ppm. The light curve cadence and duration are similar to a single-sector TESS FFI observation. The injected planet has an orbital period of two days and a transit duration of two hours. The top row shows the simulated light curve (left) and its autocorrelation function (right). The second row shows the BLS (left) and TCF (right) periodograms. The red curve gives the *cobs* median fit to the periodogram powers. A rug plot (small vertical marks on the x-axis) shows the location of the knots used for the median fit. Annotations give the SNR, period, and depth obtained from the periodogram. The third row gives histograms of the BLS (left) and TCF (right) power values. The fourth and fifth rows show the periodograms and the corresponding histograms after standardization. Annotation in the fourth row gives the FAP value of the peak in the standardized periodogram

BLS (FAP =  $4 \times 10^{-2}$ ). BLS shows strong trends and heteroscedasticity in the periodogram, while these problems are milder for TCF. Altogether, the ARIMA fitting and TCF periodogram are much better behaved than the BLS periodogram in the presence of autocorrelated noise.

We thus see a big difference in periodogram noise characteristics in response to light curves with Gaussian *vs.* autoregressive noise. The BLS and TCF periodograms share basic properties – mild trends and heteroscedasticity – for Gaussian noise. The TCF periodograms have a similar structure even for autoregressive noise, as the autoregression is effectively removed by the ARIMA

modeling that precedes TCF. However, Gaussian Processes (or similar nonparametric local) regression applied before BLS leaves significant autocorrelation if it was present in the original light curve. The BLS periodogram in Figures 3-4 thereby exhibit undesirable strong behaviors not present in Figures 1-2 with Gaussian noise. Consequently, BLS has less ability to detect small planets if autocorrelation in the light curve still persists after detrending.

We thus find, for this single simulation, that TCF detects small planets more effectively *both* for simulated light curves with Gaussian noise (Figures 1-2) and with autoregressive noise (Figures 3-4).

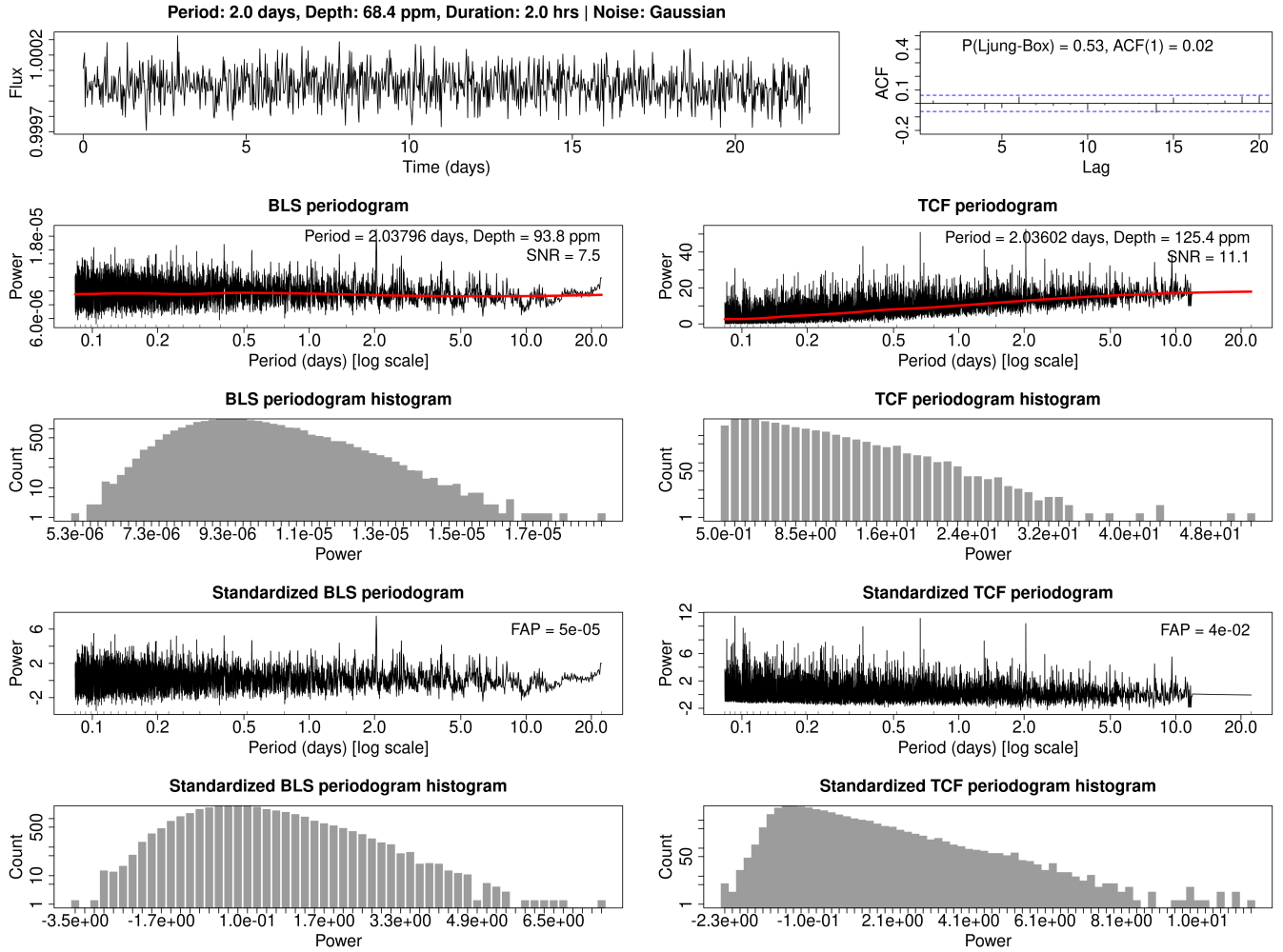


**Figure 2.** Periodogram analysis for Gaussian noise and a smaller planet with injected transit depth 68 ppm. See Figure 1 for a description of the panels.

We can finally inquire into the accuracy of the transiting planet depth obtained from the BLS and TCF periodograms. For Gaussian noise, depth estimates in both periodograms overestimate the simulated depths. The situation differs for autoregressive noise, where the TCF underestimates the true depth. Inaccuracies in TCF depth estimation may have several causes: (a) incorporation of some transit signal into the ARMA fit can reduce the estimated depth; (b) “over-differencing” by ARIMA can produce an anti-correlation at lag = 1 and increase the estimated depth; and (c) inaccurate registration of the cadence with respect to the transit ingress and egress can reduce the double-spike signal and estimated depth. See Figure 7 in Melton et al. (2023a) and also Melton et al. (2023b) for more discussion.

These problems with TCF depth estimation were noted by Caceres et al. (2019b) and Melton et al. (2023b) in their Kepler and TESS applications, requiring improvement during the vetting phase of analysis. Diffi-

culties with transit depth estimation also arise in BLS transit fitting, as discussed by Kovács et al. (2002) and Ofir (2014). Altogether, planet parameters derived from periodograms alone may be inaccurate in complicated ways.

As expected from the mathematical discussion in §2, we can visually see in rows 4-5 of Figures 1-4 that the FAP significance calculation based on EVT depends on the rightmost tail region of the periodogram power distributions. The histograms also provide information about the overall noise characteristics of the periodogram. Ideally, for a single true periodic signal, the rightmost bin in the histograms would be a single isolated count<sup>6</sup>. The presence of histogram values crowded near the maximum indicates that spurious peaks con-

<sup>6</sup> Since we oversample the periodogram with  $K = 2$  in these simulations, often the principal peak has Count = 2 rather than 1 in the rightmost (or maximum) bin of the periodogram histograms.

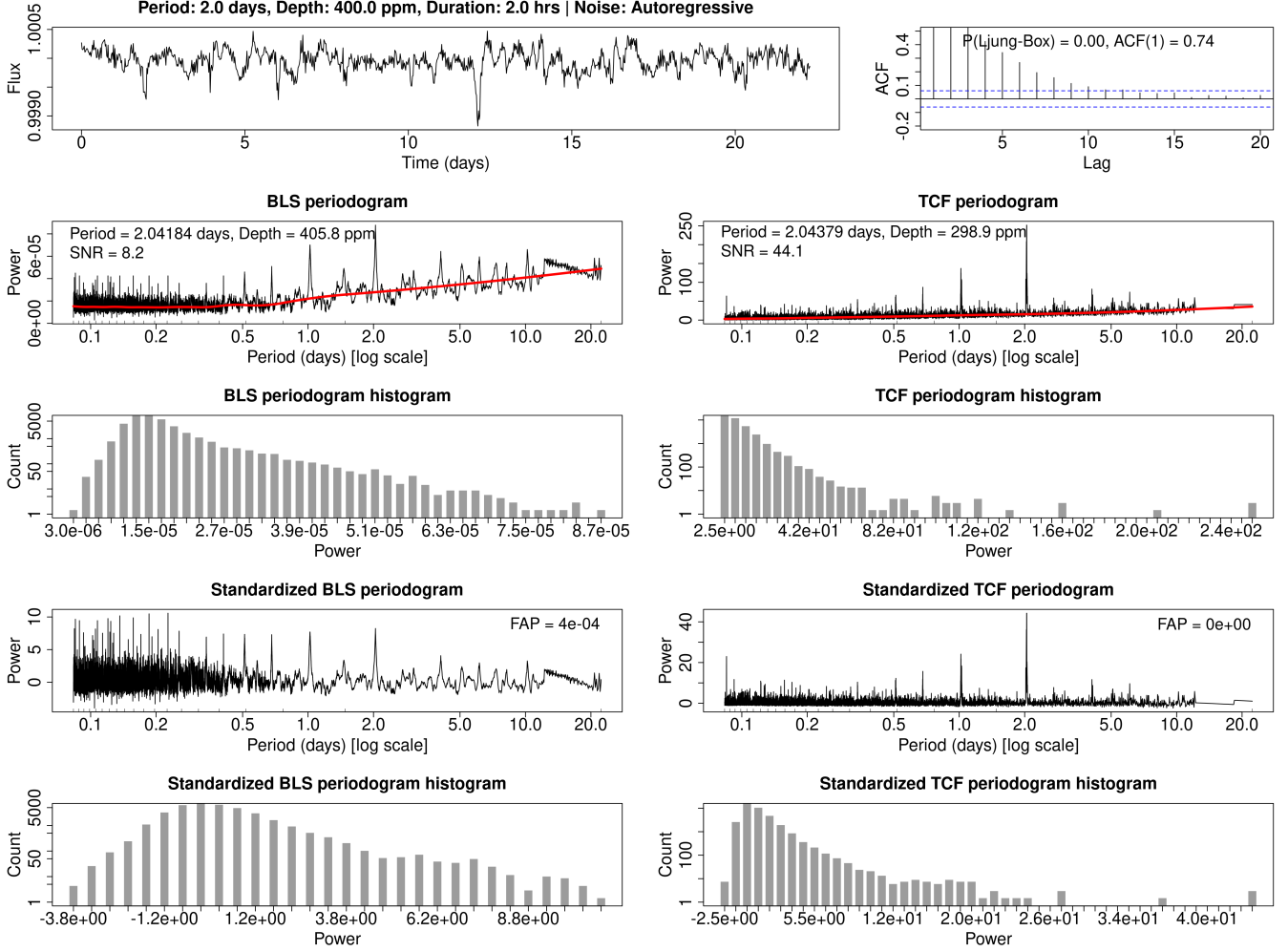


**Figure 3.** Periodogram analysis with autoregressive noise. Here the injected transit depth is 400 ppm. See Figure 1 for a description of the panels.

fusing the true signal are present, either from aliases or noise. The shape of the histograms for the bulk of noise values of the BLS and TCF periodograms differ considerably; both have strongly skewed, non-Gaussian distributions. However, this distribution pattern does not affect the FAP significance analyses.

The FAP metric results indicate that BLS is more sensitive than TCF under Gaussian noise situations (Figure 2), but it is less effective than TCF under autoregressive noise situations (Figure 4). However, TCF outperforms BLS using the SNR metric for Gaussian and autoregressive noise. This suggests that both metrics present contrasting perspectives.

The FAP values shown in the plots correspond to a single realization of noise used to create the light curves. In practice, we have observed that the FAPs change when different noise realizations are used (see §5.1 for more details).

An effect worth pointing out is that post-standardization, the local periodogram noise at shorter periods is enhanced, which arises due to the heteroscedastic noise pattern of the periodogram. A modified windowed approach could be used to mitigate this issue to some extent; however, we do not deal with it here since the FAP calculation does not consider the periodogram noise.

A few other remarks are as follows:

1. We have also verified the  $P^{-1/3}$  and  $P^{-1/2}$  dependence of BLS and TCF periodogram peak, where  $P$  is the planet period, as described in [Caceres et al. \(2019a\)](#). To achieve this, we simulated three planets with the same transit depth and duration but varying the period and number of transits so that the total length of the light curve

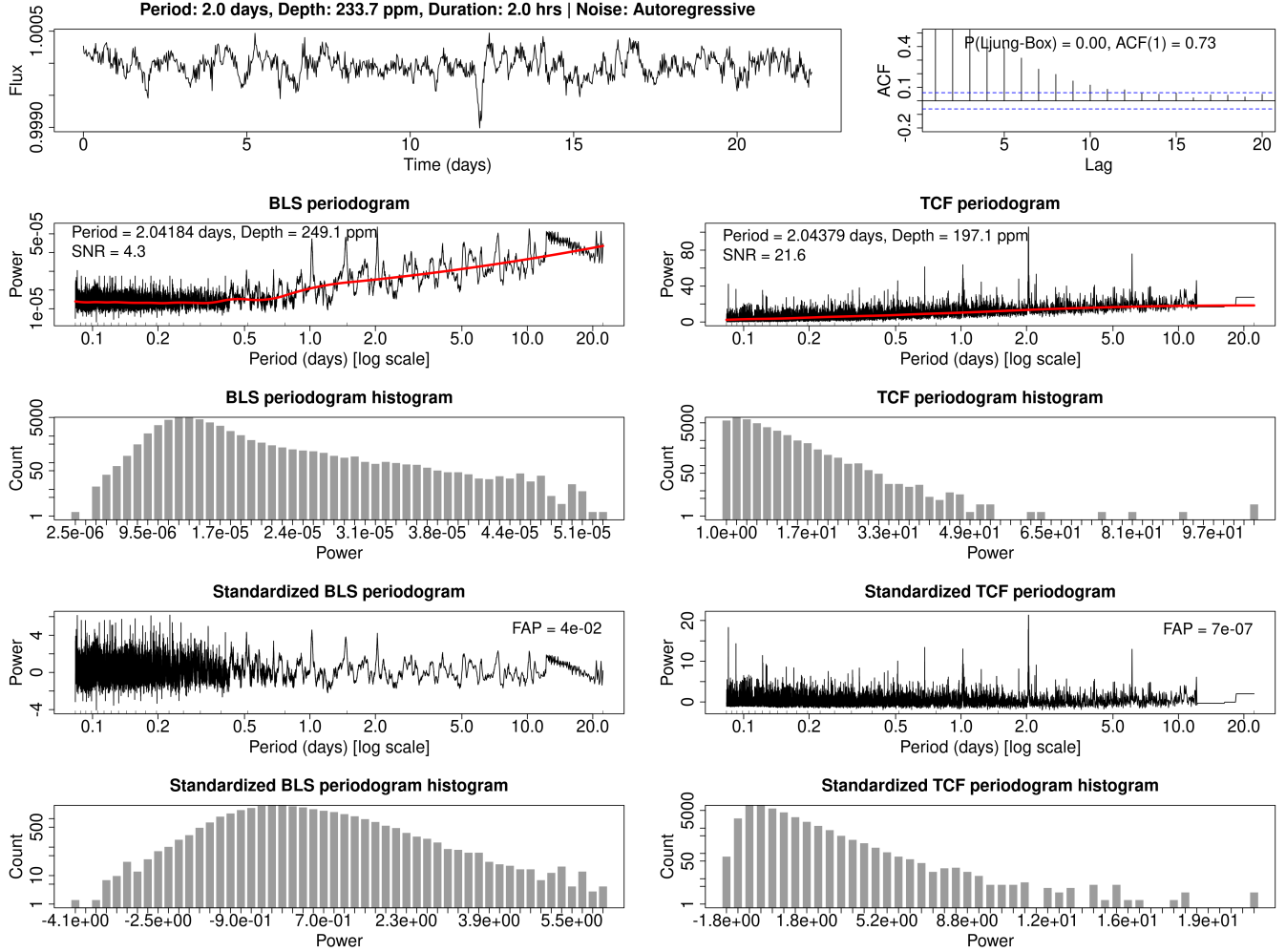


**Figure 4.** Periodogram analysis with autoregressive noise and a smaller injected planet with 234 ppm. See Figure 1 for a description of the panels.

- remains approximately constant<sup>7</sup>. The BLS and TCF periodogram peak powers scale as 1:0.48:0.21 and 1:0.41:0.14, which is approximately similar to  $P^{-1/3}$  and  $P^{-1/2}$ , respectively.
- Another noteworthy observation in the autoregressive case (Figures 3–4) is that the widths of the BLS periodogram peaks are larger than TCF.
  - It is important to note that the comparison of BLS and TCF presented in this paper is, in fact, a comparison of (a) Gaussian Processes regression + BLS and (b) ARIMA + TCF instead of BLS and TCF themselves. One might argue that a more

faithful comparison should consider (a) ARMA + BLS and (b) ARIMA + TCF so that the actual behaviors of periodograms are apparent. However, we have found ARMA + BLS ineffective in detecting small planets, likely because ARMA fits typically capture the transits along with the non-transit, stellar autocorrelation. ARIMA + TCF does not suffer from this issue since there are negligible transit points to fit an ARMA model on the differenced light curve.

## 5. PERIODOGRAM SENSITIVITIES FOR A RANGE OF PLANET PROPERTIES

### 5.1. Calculations

We generate simulated light curves for a range of planet and light curve properties following procedures described in §3.1. All light curves in this section have a 0.5 hr cadence. Noise characteristics are Gaussian or autoregressive following equation (5). Injected planets

<sup>7</sup> Note that the dependence mentioned in Caceres et al. (2019a) was concerned with real observational scenarios. So increasing the period should be accompanied by decreasing the number of transits in our simulation code to ensure the total length of observation remains constant. This differs from the experiments performed in Figure 6.

have trapezoidal transits with 0.5 hr ingress and egress. Computation of the BLS periodogram is a modified version of the original Fortran’77 BLS routine that accounts for edge effects and uses binning for computational efficiency (Kovács et al. 2016). The TCF implementation is the Fortran code at Caceres & Feigelson (2022) with minor modification<sup>8</sup>. The SNR metric is calculated using equation 6, and the FAP metric is calculated as described in §3.2 with  $K = 2$ ,  $R = 300$ , and  $L = 300$ . BLS and TCF periodograms are calculated using uniform frequency sampling<sup>9</sup>.

To compare the performance of periodograms under different conditions, we define a threshold called “minimum detectable depth” (MDD) of a small planet based on the SNR and FAP metrics. No clear consensus has emerged in the research community on the best thresholds that balance sensitivity for small planet detection against False Alarm reports. SNR thresholds used for (often standardized) BLS periodograms include  $\text{SNR} > 6$  (Kovács et al. 2002),  $\text{SNR} > 15$  (Ofir 2014),  $\text{SNR} > 9$  (Vanderburg et al. 2016), and  $\text{SNR} > 5$  (Shallue & Vanderburg 2018). FAP thresholds are widely used for planet detection using Lomb-Scargle or BLS periodograms with values typically ranging over  $0.001 < \text{FAP} < 0.01$  (e.g., Maxted et al. 2011; Lund et al. 2014). The threshold  $\text{FAP} = 0.003$  corresponding to the Gaussian  $3\sigma$  criterion lies in this range.

Since our scientific goal here is to maximize sensitivity for small planets and not to minimize False Alarms, we use relatively low thresholds here<sup>10</sup>. We define the MDD of a small simulated planet to be the transit depth at which  $\text{SNR} > 6$  or  $\text{FAP} < 0.01$  depending on whether FAP or SNR is used. We calculate MDD values for chosen properties of the light curve or planet properties with trial planet injections of different depths, and the MDD is the lowest depth at which the planet depth is still significant, as quantified by the FAP or SNR of the periodogram peak. Our internal tests have shown that, for some cases, the FAPs of periodogram peaks change considerably across different noise realizations of the light curve but are stable in many other cases. The instabil-

ity of FAPs across different realizations poses no issues for very high or very low FAPs but only for FAPs near the set threshold, 0.01. Subsequently, the MDD values are averaged across ten distinct noise realizations in all cases to get more reliable sensitivities. Planet properties cover the range of Kepler-discovered planets that might be detected in a single sector of TESS observations.

We note that some of our simulations have the number of transits as a tunable parameter, as this most clearly reveals differences between periodogram performance. This differs from observational surveys, where the availability of time for observing a host star, rather than the number of transits, is known beforehand.

## 5.2. Results

Figures 5-6 compare BLS and TCF as a function of properties of the light curve (number of transits, Gaussian *vs.* autoregressive noise), properties of injected planets (orbital period, transit duration), and statistical metric for planet detection (SNR *vs.* FAP).

The four panels of Figure 5 give insight into a critical effect discussed in §4: the sensitivity of the BLS and TCF periodograms is reversed depending on the nature of the light curve noise and chosen detection metric. For Gaussian noise and the FAP metric (upper left panel), BLS is more sensitive than TCF (the blue curve lies below the orange curve). The periodogram sensitivities are similar for autoregressive noise using the FAP metric, while TCF is considerably more sensitive when the SNR metric is used. Differences are most substantial when fewer transits are present; the choice of periodogram and detection metric becomes unimportant for short orbital periods embedded in long-duration light curves since the number of transits in such cases is sufficiently large.

As expected, sensitivity to small planets improves by extending light curves to include more transits; more points are available for building up the box-like transit signal for BLS and the double-spike signal for TCF. However, the improvement ceases after sufficient transits are observed, as both periodograms reach a fixed MDD. In these simulations with Gaussian noise  $\sigma = 100$  ppm, we set this limit to  $\text{MDD} \simeq 50$  ppm (horizontal dashed lines). TCF’s periodogram peak has an SNR more significant than the threshold, 6, even with two transits, as seen in Figure 5. A larger SNR threshold could increase TCF’s MDD for the two-transits case. Overall, the FAP metric is less effective than the SNR metric for small planet detection when the number of transits is small.

Figure 6 compares the sensitivity of the BLS and TCF periodograms to the orbital period and transit dura-

<sup>8</sup> This code can be obtained at <https://github.com/Yash-10/ARPS-Periodogram-Comparison>

<sup>9</sup> We use constant frequency intervals in our periodograms instead of frequency intervals dependent on frequency as used by Ofir (2014) and Caceres et al. (2019a). Such a choice wastes some computational resources but should have little effect on the accuracy of the periodograms.

<sup>10</sup> The non-parametric bootstrap + GEV procedure described in §3.3 yields a conservative FAP estimate (higher FAPs than expected), so it is naturally beneficial for optimizing small planet detection

tion. For most combinations of light curve noise characteristics and detection metrics, the MDD does not exhibit strong dependencies on these orbital properties. BLS’s sensitivity shows some benefit from longer duration transits; this effect is expected as BLS has more points to fit the box with its least squares algorithm. The TCF algorithm considers only the double spikes from ingress and egress and is thus not sensitive to transit duration (provided the period and number of transits are fixed).

The primary trend seen in Figure 6 is the deterioration in MDD for the BLS periodogram in the presence of autoregressive noise (blue curve in the right panels, first and second rows). We suspect this arises from the timescale of the autoregressive component we added to the light curve noise compared to the timescale of the orbital period. For  $P = 0.5$  days, the variability structure covers a wide duty cycle in the folded light curve. However, for  $P = 7$  days, the structure is confined to a narrow range in phases that mimic planetary transits. This points to the importance of effectively removing correlation in the light curve on timescales comparable to a transit duration. On the other hand, the ARIMA-TCF procedure removed short-memory autocorrelation and ignored the relationship between period and transit duration. It thus has near-optimal MDD performance for the full range of periods for the SNR metric (orange curve in the right panel, second row). TCF benefits from longer-period transits using the FAP metric. In contrast, BLS only benefits when the noise is Gaussian and instead deteriorates for autoregressive noise (orange and blue curves in the two columns in the top row for TCF and BLS, respectively). Overall, the number of transits, not the period and duration (when the number of transits is fixed) is the dominant factor affecting the sensitivity of BLS and TCF periodograms.

## 6. APPLICATION TO TESS LIGHT CURVES

To complement our comparison of the BLS and TCF periodograms in simulated lightcurves (§§3-5), we apply the procedures to four TESS FFI light curves drawn from the DTARPS survey (Melton et al. 2023a,b,c) that contain true known small exoplanets. Trends in these light curves have been removed using splines; however, we still preprocess the light curve using Gaussian Processes regression to maintain an analysis procedure similar to our simulations above<sup>11</sup>. We conduct the analysis without using the known period.

The test performed here uses realistic rather than simplified light curves, no control over the noise level or characteristics, and gaps in observations from satellite operations. Since ARIMA requires uniformly-spaced time series, one can consider the observations evenly spaced with missing data points (Feigelson et al. 2018). The data gaps create spurious structures in periodograms, which may particularly affect the GEV fits and associated FAPs (Süveges 2014).

Figures 7-10 and Table 1 show the results of the periodogram analysis on the four TESS light curves. One can see that both BLS and TCF periodograms obtained spectral peaks at the true orbital periods in all four cases. Other effects in Table 1 are very similar to those found in the simulations. BLS and TCF estimated transit depths tend to underestimate true depths. All peak SNR values are much higher for TCF than BLS, while peak FAP values are typically more significant for BLS than TCF.

The autocorrelation functions in Figures 7-10 show mild anticorrelations with lags up to 10 hours. Consequently, the periodograms show only mild trends and heteroscedasticity with the period. The expected aliases associated with the true period are seen in both periodograms. The TCF periodogram generally has smaller noise, giving it a higher peak SNR than BLS. The mild autocorrelation observed in these four cases also suggests that the expected comparisons should follow more closely to the Gaussian simulations than the autoregressive simulations, which are observed here.

We thus find a complete validation of the simulation results in these real TESS FFI light curves.

<sup>11</sup> We observed negligible difference in the final results when Gaussian Processes regression is omitted here.

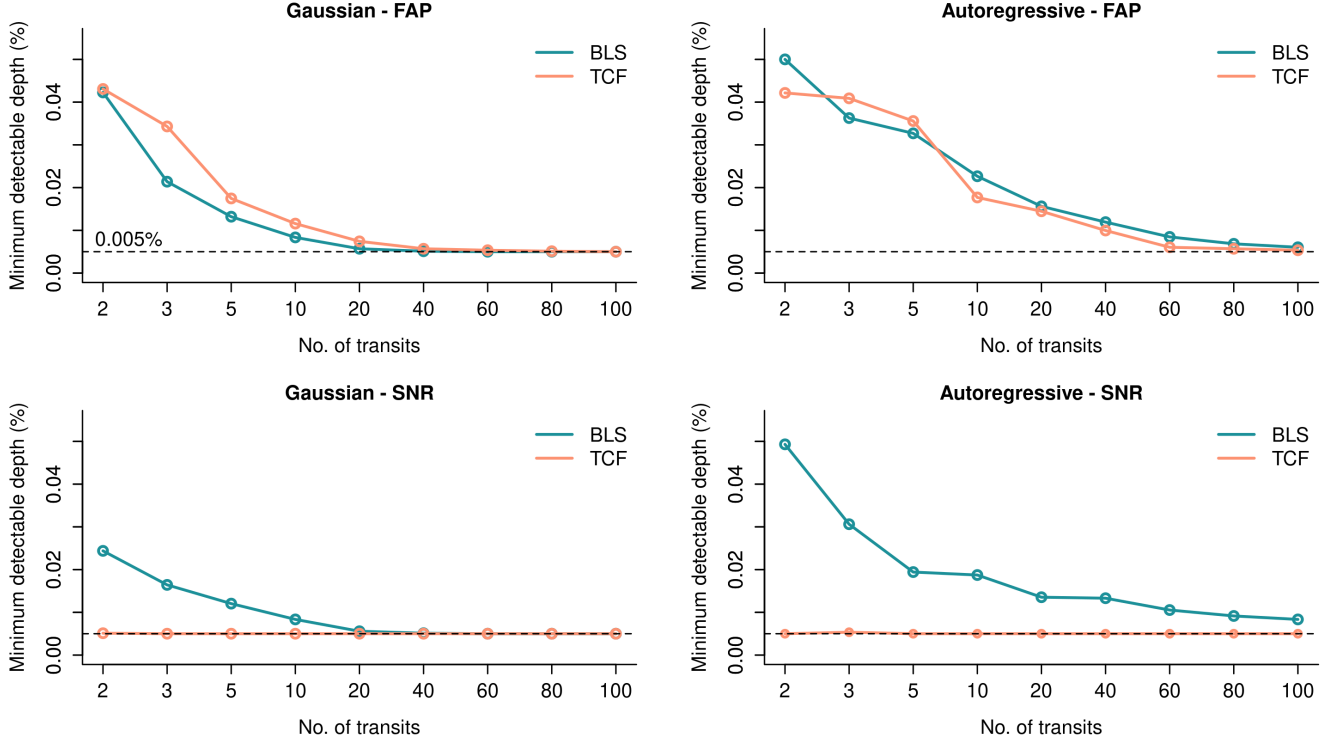


**Figure 5.** Minimum detectable depth (MDD) (in percent of the stellar brightness) as a function of the number of transits. The injected planet has a one-day period and a two-hour transit duration. Two metrics are shown: FAP based on extreme value theory on standardized periodograms (top row) and signal-to-noise ratio on detrended periodograms (bottom row). Light curves have Gaussian white noise (left column) and autoregressive noise (right column). Each panel shows the MDD for the BLS (blue curve) and TCF (orange curve) periodograms. The horizontal dashed line corresponds to  $MDD = 0.005\%$  to guide the eye.

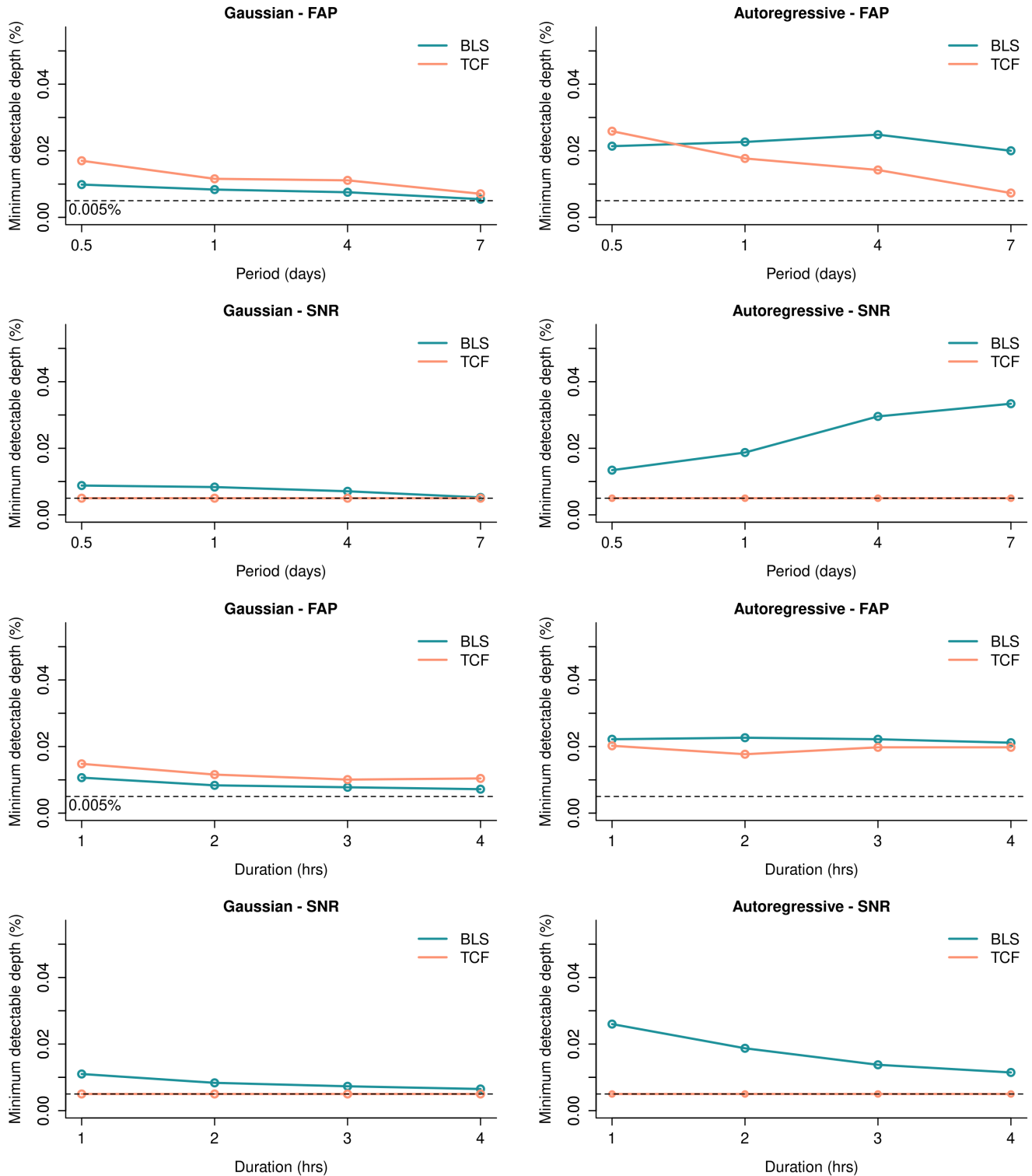


**Figure 6.** Minimum detectable depth (MDD) as a function of transit period (top rows) and duration (bottom rows). Simulations assume ten transits, transit duration = 2 hrs for the comparison using period, and period = 1 day for the comparison using transit duration. See Figure 5 for panel details.

**Table 1.** Periodogram Performance for Four TESS Planet Candidates

TARPS	TIC	Name/Disp	Period	Depth	SNR	FAP
(1)	(2)	(3)	(4)	(5)	(6)	(7)
27	22221375	TOI 652.01	3.99	300	...	...
	BLS	DTARPS 27	3.98387	~322	17.4	$< 10^{-6}$
	TCF	CP	3.98205	~310	32.9	$< 10^{-6}$
98	78669098	...	0.57787	700	...	...
	BLS	DTARPS 98	0.57764	~477	24.2	$< 10^{-6}$
	TCF	...	0.57778	~530	63.7	$< 10^{-6}$
103	89020549	TOI 2336.01	2.11173	1200	...	...
	BLS	DTARPS 103	2.11076	~1048	18.8	$< 10^{-6}$
	TCF	CP	2.11045	~986	22.6	$10^{-5}$
197	176685457	TOI 1935.01	4.43427	6600	...	...
	BLS	DTARPS 197	4.43031	~4035	10.2	$6 \times 10^{-4}$
	TCF	CP	4.44109	~3185	18.9	$3 \times 10^{-3}$

NOTE— The associated periodograms are shown in Figures 7-10.

Col. 1: DIAmante AutoRegressive Planet Search identifier from Melton et al. (2023b).

Col. 2: TESS Input Catalog identifier.

Col. 3: Names and Disposition. Row 1 gives the TOI designation from <https://tess.mit.edu/toi-releases/>. Row 2 gives the DTARPS designation from Melton et al. (2023a) based on ARIMA+TCF analysis. Row 3 gives the disposition from <https://exoplanetarchive.ipac.caltech.edu> where CP = Confirmed Planet. Col. 4. The orbital period from the NASA Exoplanet Archive (first line) and the two periodograms (second and third line).

Col. 5: Depth in ppm.

Col. 6: Peak Signal-to-Noise Ratio for the detrended periodogram.

Col. 7: Extreme Value Theory False Alarm Probability for the standardized periodogram.



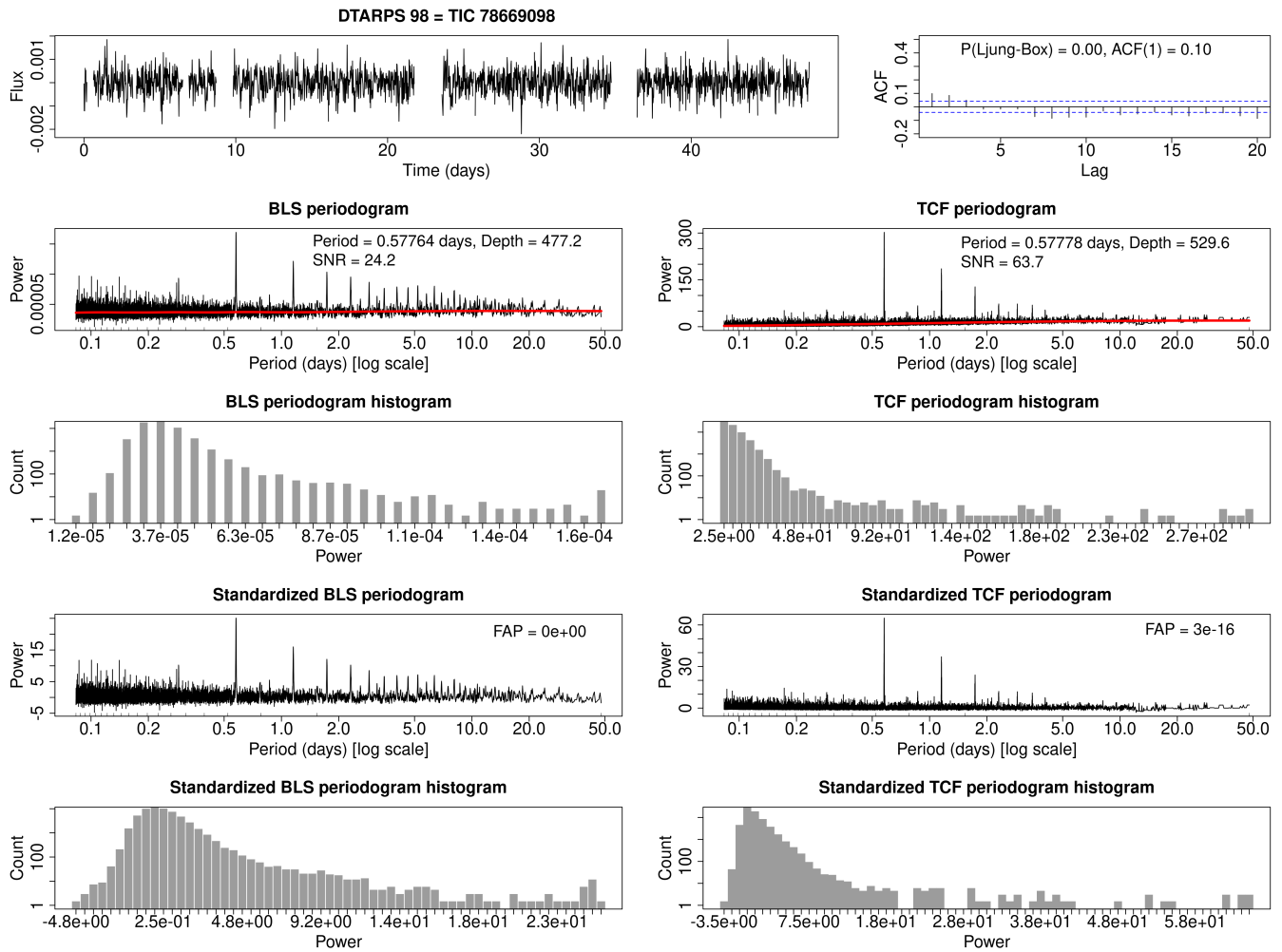


**Figure 8.** Example 2 of a TESS Year 1 light curve and the corresponding periodograms and histograms. See Figure 7 for a description of the panels.

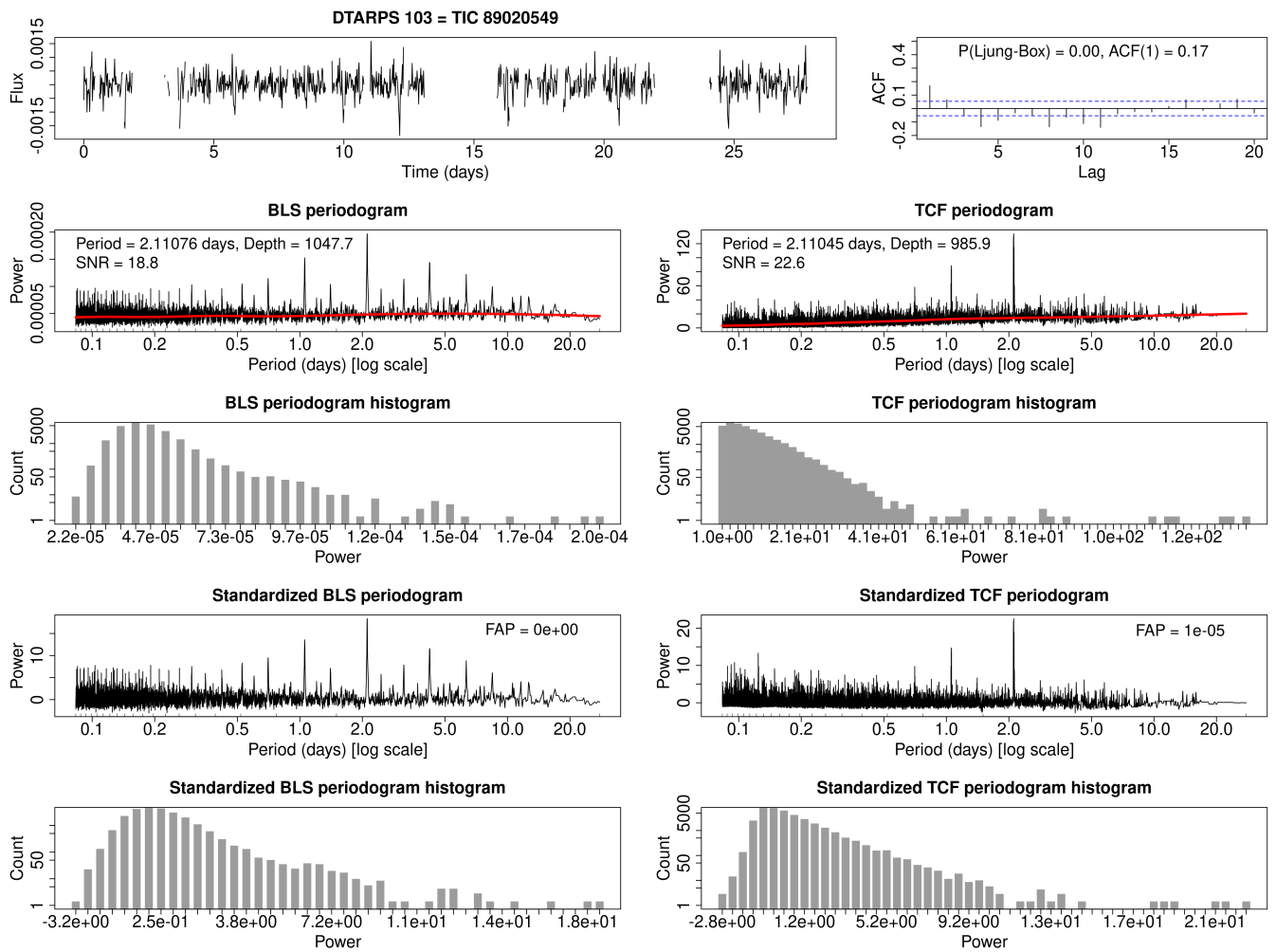


**Figure 9.** Example 3 of a TESS Year 1 light curve and the corresponding periodograms and histograms. See Figure 7 for a description of the panels.

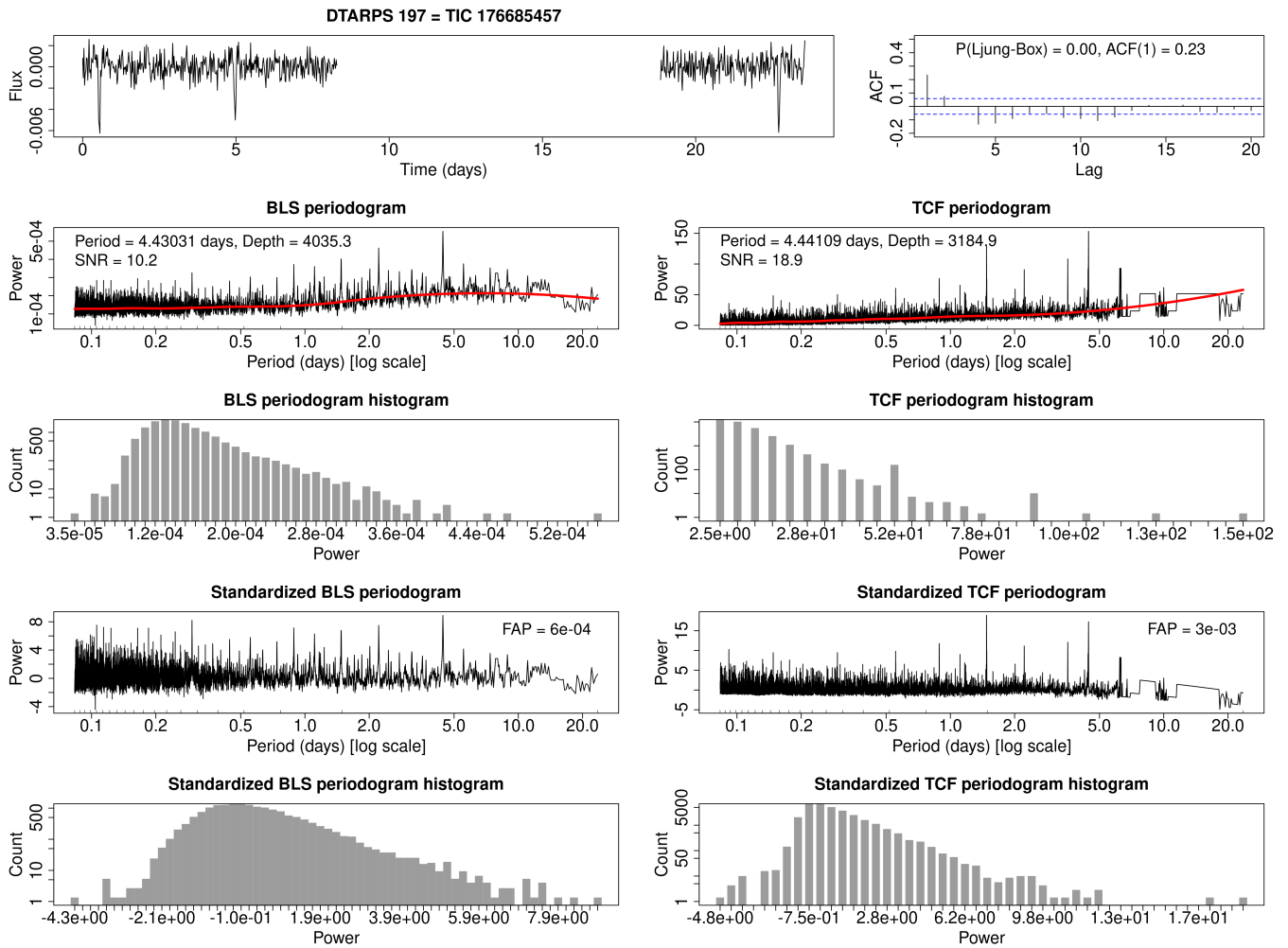


**Figure 10.** Example 4 of a TESS Year 1 light curve and the corresponding periodograms and histograms. See Figure 7 for a description of the panels.

## 7. DISCUSSION

### 7.1. Summary of the study

This methodological paper thoroughly compares the Box-Least Squares (BLS) and Transit Comb Filter (TCF) periodograms to optimize the detection of small exoplanets from light curves with regular cadences as obtained from space-based surveys. The analysis has several steps:

1. Tests are first conducted on simulated light curves with Gaussian and autoregressive noise by varying the number of transits, planet period, and transit duration (§3). The simulated light curves resemble single-sector TESS observations. The analysis is repeated for four observed TESS light curves with known small planetary transit signals (§6).
2. The light curves are detrended with a Gaussian Processes regression model prior to applying the BLS periodogram and with an ARIMA regression model prior to applying the TCF periodogram (§3.1).
3. Two statistical metrics are applied to decide whether a periodogram peak represents a true planetary signal: a Signal-to-Noise Ratio (SNR) measured locally in the periodogram using a robust noise measure and a False Alarm Probability (FAP) based on extreme value theory (§3.2-3.3). In the latter case, a Generalized Extreme Value (GEV, §2) statistical model is fitted to peaks of bootstrapped periodograms calculated using only a portion of the frequency range for alleviating high computational costs, as proposed by Süveges (2014).
4. The sensitivity of a given periodogram is quantified with a Minimum Detection Depth (MDD) measure defined as the smallest statistically significant transit depth (§5).

Our most noteworthy finding for both simulated and observed light curves is that TCF’s periodogram peak shows larger SNR than BLS in all experimented cases when the number of transits in the light curve is below  $\sim 20$  ( $\sim 100$ ) transits for Gaussian (autoregressive) noise (§5). This indicates that the TCF periodogram following ARIMA modeling is more sensitive to small planets than BLS (following some local regression procedures like Gaussian Processes or spline fitting) using the SNR criterion. TCF shows no degradation in sensitivity to small planets as the number of transits in the light curve drops, even for only 2 – 3 transits.

It may seem surprising that TCF outperforms BLS even for the pure Gaussian noise simulations, as a least squares procedure gives a maximum likelihood estimator according to the Gauss-Markov Theorem. However, the theorem only applies to Gaussian noise, while periodograms have strongly non-Gaussian power distributions, as seen in the histograms of periodogram power values. We discuss this issue below (§7.2).

We find that the FAP and SNR metrics do not lead to the same conclusion but instead contrast each other. Experiments on Gaussian noise suggest that BLS is slightly more sensitive than TCF using the FAP criterion, whereas TCF is more sensitive using the SNR criterion. For the FAP metric and light curves with autoregressive noise (upper right panel of Figure 5), the sensitivities of both periodograms using the FAP criterion are degraded compared to the case of pure Gaussian noise light curves, particularly when few transits are present. However, this is not a critical problem, as the SNR metric is remarkably unaffected by the number of transits for the TCF periodogram.

The four TESS light curves analyzed in section 6 have milder autocorrelation than in our simulations but are significant enough to distinguish it from white Gaussian noise. All four planets readily passed our significance criteria (periodogram peak FAP  $< 0.01$  or SNR  $> 6$ ) for both BLS and TCF with the correct orbital periods.

Altogether, the most sensitive approach to small planet discovery is using the Transit Comb Filter periodogram preceded by ARIMA modeling of the light curve and a robust Signal-to-Noise Ratio metric. These findings explain why TCF had high sensitivity to small planets in previous studies: [Caceres et al. \(2019b\)](#) who reported 97 Earth- and Mars-sized planetary candidates from the 4-year Kepler data, and [Melton et al. \(2023c, Figure 16\)](#) who reported hundreds of candidate planets substantially smaller than Confirmed Planets in the Year 1 TESS survey. As investigated by our internal experiments, an advantage of SNR over FAP is that while the latter tends to fluctuate non-trivially across multiple simulated noise realizations (§5.1), the former was found to be relatively more stable.

### 7.2. Why does BLS perform so poorly?

Ideally, both simulated noise models (Gaussian and autoregressive) should have resulted in similar conclusions since BLS and TCF are preceded by detrending procedures that should have removed any correlation structure from the light curve. However, our findings show that BLS (preceded by Gaussian Processes regression detrending) is less sensitive to small planets than TCF (preceded by ARIMA regression detrending). We

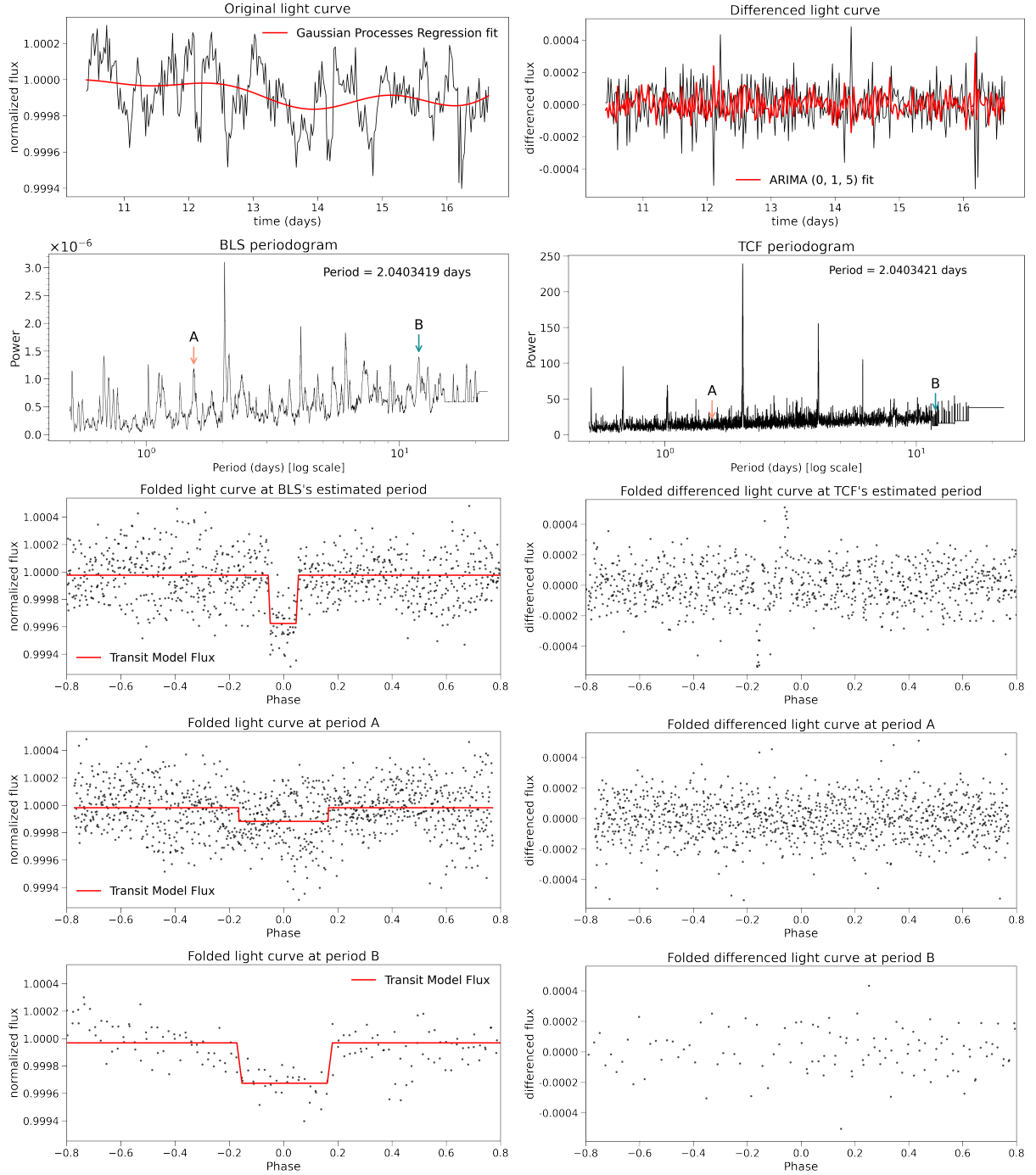


**Figure 11.** Illustration of BLS (left panels) and TCF (right panels) analysis of a simulated light curve with a  $P=2.00$  day transiting planet superposed on autocorrelated noise. *First row:* Zoom of several days of the light curve with the Gaussian Processes Regression fit overlaid (left) and the same light curve after differencing with the ARMA fit overlaid (right). *Second row:* Periodograms of the entire simulated light curve with two BLS false peaks 'A' and 'B' marked. *Third row:* Folded light curves for the true transit period. *Fourth and fifth rows:* Folded light curves of the original (left) and differenced (right) data for the false spectral peaks A and B.

investigate the causes of this difference in sensitivity with a detailed examination of the inner workings of both algorithms.

Figure 11 shows an example of a simulated planet with period = 2.00 days, transit duration = 2.00 hrs, depth = 0.04%, ten transits in the light curve, and autoregressive noise with ARMA (3, 3) from equation 5<sup>12</sup>. The depth is chosen sufficiently large so that BLS and TCF peaks are significant using the FAP and SNR criteria.

The top-left plot shows the original light curve with the Gaussian Processes Regression fit overlaid; the top-right plot shows the differenced light curve with the ARMA fit. This Gaussian Process fit clearly misses most of the short-memory structure, although different kernel hyperparameters might do a better job. The second row shows the corresponding BLS and TCF periodograms. The same set of test periods is used; here, we omit the Gaussian Processing detrending to better highlight BLS’s characteristics in the case of short-memory autocorrelation. The BLS periodogram exhibits higher and spikier noise and a stronger rising trend with period than the TCF periodogram, as seen earlier in Figures 1-4 and Figures 7-10.

The fourth and fifth rows of Figure 11 examine two false peaks marked by labels “A” and “B” corresponding to shorter and longer periods in the periodograms, respectively. The folded light curves for the correct period clearly show a box-like transit for BLS and a double spike for TCF (third row). Since periods A and B are not the true period, their light curves should not possess box-like shapes for BLS and double-spike for TCF. However, the fourth and fifth rows of Figure 11 illustrate that model fitted by BLS tends to capture chance alignments of outliers or autocorrelated ripples even when the folded light curve possesses no transits. While TCF can also match a double spike pattern at non-transit periods, it is used only when the autocorrelation is removed via ARIMA modeling. TCF only considers extreme points in the differenced light curve that proves to be less susceptible to random chance alignments.

We infer from Figure 11 that BLS periodograms are often noisier than TCF periodograms, particularly for light curves with short-memory autocorrelation remaining after inadequate detrending, because chance alignments of the structure can easily mimic box-like shapes. On the other hand, the double-spike structure matched by the TCF algorithms is difficult to reproduce by au-

tocorrelation alone, so the TCF periodogram noise is better behaved. The trend of increasing BLS power as the period increases for all periods without true periodic signals can be attributed to the weaker dilution of autocorrelated patterns in the folded light curves. This can be seen by comparing the higher depth of the false box in the fifth row compared to the false box in the fourth row.

It is reasonable that the BLS algorithm (with a standard detrender like Gaussian Processes regression) produces more noise than the TCF algorithm (with an ARIMA detrender designed to remove stochastic short-memory autocorrelation) when the detrended light curve has significant autocorrelation. However, we are surprised that TCF can outperform BLS with the signal-to-noise ratio metric when the light curve is mostly white Gaussian noise (Figures 1-2 and the lower-left panel of Figure 5). We believe the TCF algorithm is more stable because it seeks a distinctive double-spike pattern of a few brightness outliers, which are sparse and unlikely to be aligned in light curves folded with random periods.

### 7.3. Advice for transit searches

Figures 5-6 have shown that a combination of TCF with the SNR metric achieves excellent sensitivity to small transiting planets for a wide range of transit periods and durations, whereas the other combinations of detection methods (TCF-FAP, BLS-FAP, and BLS-SNR) were relatively less sensitive.

Based on this result, we recommend the following procedure for small planet detection from a transit survey:

**Preprocess the light curve:** Compute the nonparametric autocorrelation function of the light curve. In the case of irregularly-spaced light curves, the traditional ACF estimation as used in this study may not be defined, so some modifications are needed (see, e.g., Scargle 1989; Andronov & Chinarova 2005). If the ACF deviates significantly from white noise (based on the Durbin-Watson and Ljung-Box hypothesis tests), then fit the best ARIMA model with complexity determined by the Akaike Information Criterion. A single differencing step should be used so that box-shaped transits

<sup>12</sup> We used the `Lightkurve` Python package (Lightkurve Collaboration et al. 2018b), version 2.3.0 for generating the folded light curves, showing the BLS transit models, and for the corresponding plots.

are converted to double-spike patterns<sup>13</sup>. Repeat the autocorrelation function of the residuals to see whether they approach uncorrelated white noise.

**Compute the TCF periodogram:** This search for periodic double-spike patterns is calculated on the ARIMA residuals for a chosen range of periods with an oversampling of trial periods so that true spectral peaks are not missed. The periodogram is standardized in a robust fashion (footnote 4).

**Identify the best trial transit period:** The robust SNR metric in equation (6) is calculated for each trial period of the standardized TCF periodogram. The highest SNR peak represents the best possibility of a transiting planet detection.

**Reduce statistical False Alarms:** This is a multifaceted step that can include: an examination of the periodogram for noise peaks comparable to the best peak, examination of folded light curves for patterns inconsistent with true periodic photometric dips, and construction of simulated light curves of the suspected transit. The periodograms of the simulations should be examined for alias structure and MDD sensitivity for comparison with the observed periodogram.

**Reduce astronomical False Positives:** These steps – discussed by Guerrero et al. (2021), Melton et al. (2023a) and others mentioned in §1 – lie beyond the scope of our discussion here.

These suggestions are summarized in Figure 12. However, it should not be considered the ultimate guide. In particular, we recommend making new versions of the MDD plots similar to Figure 5 based on the characteristics of the transit survey (noise level, non-Gaussian behaviors, observation duration, etc.) under study.

<sup>13</sup> We recommend using the *auto.arima* function in the *forecast* CRAN package within the R statistical software environment described in the volume by Hyndman & Athanasopoulos (2021). The *forecast* package, downloaded  $\sim 8000$  times per day for many purposes, is highly capable and reliable. Details on the *forecast* package can be found at <https://pkg.robjhyndman.com/forecast/> and <https://cran.r-project.org/web/packages/forecast>. A complete version of our pipeline can be found at <https://github.com/Yash-10/ARPS-Periodogram-Comparison>. The specific command sequence we recommend is:

```
diff.lc = c(NA, diff(lightcurve.values)) # Single differencing operation
ARIMA.fit = auto.arima(diff.lc, stepwise=FALSE, approximation=FALSE, seasonal=FALSE, max.p=5, max.q=5, max.d=0)
# Find best fit up to complexity ARIMA(5,1,5).
```

An additional analysis procedure can be considered to help adjudicate the reality of a small planet transit signal. First, Hippke & Heller (2019) shows that incorporating astrophysical knowledge can improve sensitivity to small planets. Here the square box shape transit of BLS and TCF is curved due to stellar limb darkening. The limb darkening shape depends on the star’s effective temperature and surface gravity, which can be inferred from *Gaia* photometry and astrometry. This curved transit shape could be incorporated into a BLS algorithm or the TLS algorithm of Hippke & Heller (2019). Second, after a tentative periodicity has been identified from the TCF periodogram after ARIMA detrending, one might fit an ARIMAX model to the light curve that incorporates a deterministic box-shaped periodic transit component with the stochastic autoregressive component. This gives a new estimate of the transit depth with uncertainty based on the model Fisher information matrix. The SNR of the resulting transit depth can be beneficial for subsequent analyses. See Caceres et al. (2019a) (§3.3) for more details.

ARIMA + TCF and TLS are complementary approaches: while TLS improves the sensitivity of BLS by adding astrophysical insights, TCF is more sensitive than BLS due to an effective treatment of stellar autoregressive noise, resulting in reduced periodogram noise. The standard ARIMA + TCF procedure could be followed by TLS, a more refined periodogram incorporating limb darkening, and a self-consistent pattern of transit ingress and duration for the particular stellar and planetary inferred parameters from the standard procedure.

## 8. CONCLUSION

This paper cautions the reader about weaknesses in the sensitivity of the commonly-used BLS periodogram for detecting small planets. Problems are exacerbated when autocorrelation persists in the light curve, even after detrending. Some of the issues with BLS – trends and heteroscedastic errors – were discussed earlier by Ofir (2014), but an alternative was not proposed.

We show here that the procedure of the AutoRegressive Planet Search project (Caceres et al. 2019a) has improved performance over standard detrenders with BLS periodogram. ARIMA, a widely used method for modeling stochastic autocorrelated time series since the 1970s (Box et al. 2015), detrends both longer-term trends and stationary short memory autoregressive behaviors in the light curve. It is followed by the Transit Comb Filter that matches the sharp ingress and egress spikes in the ARIMA residuals for a trial period.

The ARIMA+TCF pipeline proves to be remarkably effective, and we show that much of the advantage

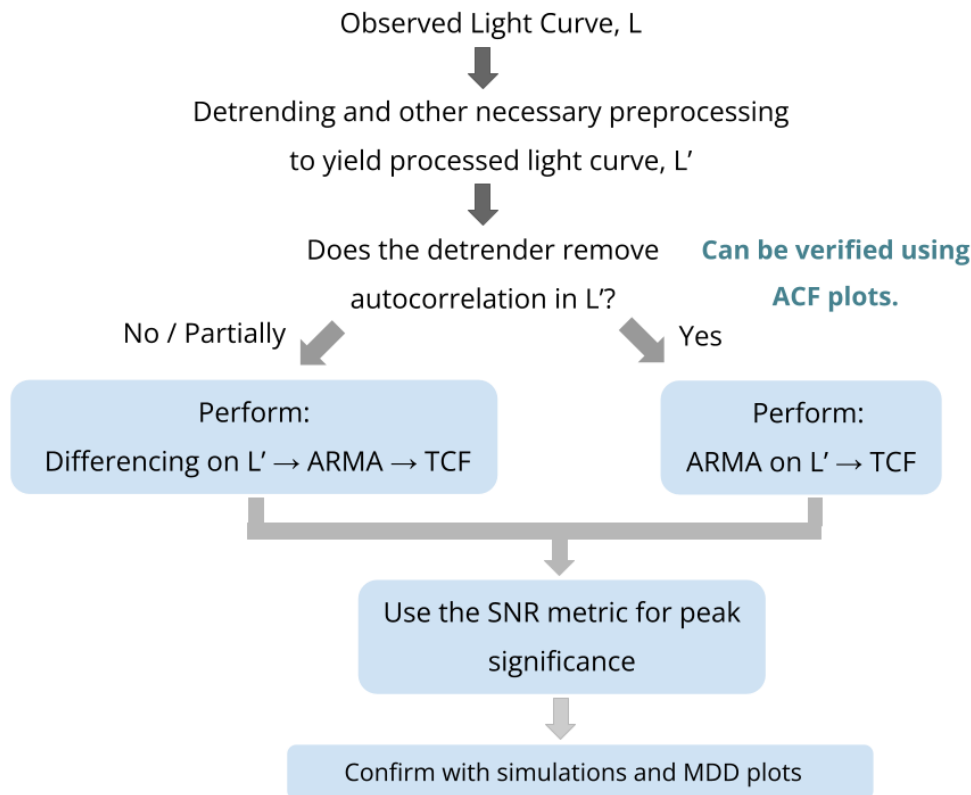


**Figure 12.** Decision tree outlining general suggestions for selecting a periodogram algorithm based on certain conditions.

emerges from the TCF periodogram. It has a lower noise with weaker spurious peaks than the BLS periodogram, even for time series with white Gaussian noise. We find the commonly used Signal-to-Noise Ratio is the preferred metric for optimizing small exoplanet detection compared to a False Alarm Probability based on extreme value theory. The latter is now often used with the Lomb-Scargle periodogram (Baluev 2008; Süveges 2014).

Our study also shows that analysis of simulations can be effective for evaluating the periodogram peak significance on observational data, particularly when complicated conditions (such as missing or autocorrelated data) in observations are present. Analysis of simulations can be used to compare any combination of periodograms. Simulations were also recommended by VanderPlas (2018) in his discussion of Lomb-Scargle periodogram peaks.

The results emphasize that effective detrending algorithms are vital to improving periodogram sensitivity. We use the classical sequence of differencing and ARMA modeling. However, combining spline or Gaussian Processes regression for longer-term trends with ARMA for short-memory stochastic autocorrelation is an intriguing possibility, which we expected to be most beneficial for BLS. However, our preliminary experiments suggest

this combination also tends to capture the transits, so BLS performance remains inferior. Any procedure seeking efficient small planet detection must avoid fitting the light curve too well.

The ARIMA method of differencing and fitting an ARMA model leaves most of the planetary signal untouched since, once the light curve is differenced, the ARMA model cannot fit the double spike since most of the in-transit points are removed. It allows the use of the TCF algorithm that gives a well-behaved periodogram. Although novel methods for removing stellar trends have been proposed (such as Alapini & Aigrain 2009), studying them in combination with periodogram analyses for detecting new, small transiting planets in upcoming exoplanet missions is essential.

In conclusion, substituting ARIMA before TCF for local regression detrenders before BLS can significantly improve the sensitivity of space-based photometric surveys for detecting small planets. The degree of improvement depends on several factors, such as the number of transits and the noise characteristics in the light curve. Prospective applications of our methodological study include existing COROT, Kepler, K2, and TESS datasets and products of ESA’s forthcoming Plato mission and NASA’s Roman Space Telescope. The discussion here does not cover all aspects of small planet detection. For

example, the incorporation of astrophysically motivated transit shapes can be combined with ARIMA + TCF to improve transit survey sensitivity further.

The AutoRegressive Planet Search project at Penn State has been funded by NASA grant 80NSSC17K0122 and NSF grant AST-1614690. We are grateful for the efforts of Elizabeth Melton (Rose-Hulman Institute of Technology) and Andrew Pellegrino (Penn State) for their substantial contributions to this project.

This research has made use of the NASA Exoplanet Archive, which is operated by the California Institute of Technology, under contract with the National Aeronautics and Space Administration under the Exoplanet Exploration Program (NASA Exoplanet Science Institute 2020). It also benefited from Lightkurve, a Python package for Kepler and TESS data analysis (Lightkurve Collaboration et al. 2018b).

*Facilities:* TESS (Ricker et al. 2015)

*Software:* BLS (Kovács et al. 2016); forecast (Hyndman et al. 2023); microbenchmark (Mersmann 2021); R (R Core Team 2022); TCF (Kovács et al. 2016). Our code implementation for estimating the statistical significance of periodogram peaks using the R programming language is available online at <https://github.com/Yash-10/ARPS-Periodogram-Comparison>.

## APPENDIX

### A. EXECUTION TIME COMPARISON OF BLS AND TCF PERIODOGRAMS

The computational execution time of the BLS and TCF calculations can be compared, and their scaling with the data set size can be established. The experiment was performed on a machine equipped with Intel(R) Xeon(R) CPU at 2.20GHz using a single CPU core. The same optimal frequency sampling is used for BLS and TCF.

We simulate light curves with Gaussian noise and ten transits of a planet producing depth = 100 ppm transits, each with 2 hours duration. To increase the data points in the light curve, the period is progressively increased while all other parameters are kept fixed—the periods used are 0.5, 1, 3, 5, 10, 20, 40, 80 days. The number of points in the light curve ranges from a few hundred to  $\sim 10^4$ .

We use the `microbenchmark` CRAN package (Mersmann 2021) to measure execution times. The execution time does not include preprocessing operations, such as ARIMA for TCF or Gaussian Processes regression before BLS; these occur much faster than the periodogram computation. For the relatively smaller periods, we use the median execution time across five different runs since we observed non-trivial differences across different runs. For the larger periods, we use the execution time from only one run.

Figure 13 shows the execution time comparison of BLS and TCF. The figure illustrates that TCF is somewhat faster than the BLS algorithm and scales as  $\mathcal{O}(N^3)$ , somewhat better than BLS with  $\mathcal{O}(N^{3.7})$ . We have not examined alternative, faster versions of the BLS algorithm such as SparseBLS (Panahi & Zucker 2021) and fBLS (Shahaf et al. 2022).

## REFERENCES

- Aigrain, S., Favata, F., & Gilmore, G. 2004, *A&A*, 414, 1139, doi: [10.1051/0004-6361:20034039](https://doi.org/10.1051/0004-6361:20034039)
- Alapini, A., & Aigrain, S. 2009, *Monthly Notices of the Royal Astronomical Society*, 397, 1591, doi: [10.1111/j.1365-2966.2009.15052.x](https://doi.org/10.1111/j.1365-2966.2009.15052.x)
- Andronov, I. L., & Chinarova, L. L. 2005, in *Astronomical Society of the Pacific Conference Series*, Vol. 334, 14th European Workshop on White Dwarfs, ed. D. Koester & S. Moehler, 659
- Asensio Ramos, A. 2007, *A&A*, 472, 293, doi: [10.1051/0004-6361:20077574](https://doi.org/10.1051/0004-6361:20077574)
- Baglin, A., Auvergne, M., Barge, P., Deleuil, M., & Michel, E. 2008, *Proceedings of the International Astronomical Union*, 4, 71–81, doi: [10.1017/S1743921308026252](https://doi.org/10.1017/S1743921308026252)
- Baluev, R. V. 2008, *Monthly Notices of the Royal Astronomical Society*, 385, 1279, doi: [10.1111/j.1365-2966.2008.12689.x](https://doi.org/10.1111/j.1365-2966.2008.12689.x)

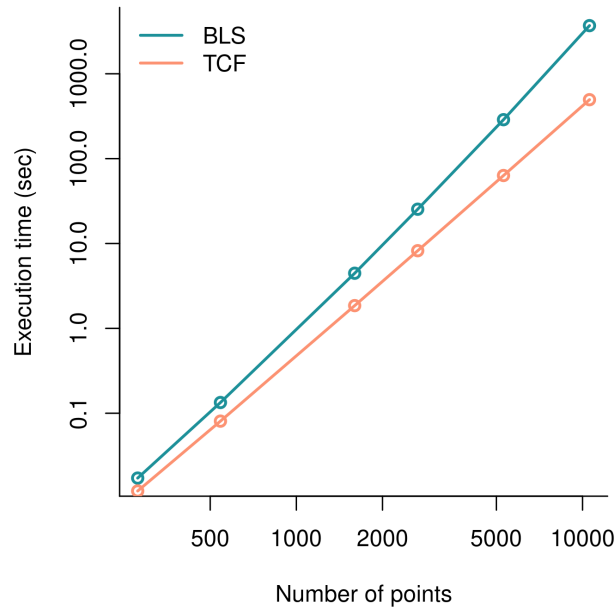


**Figure 13.** Execution time comparison of BLS and TCF as a function of the number of data points in the light curve.

- . 2013, *Monthly Notices of the Royal Astronomical Society*, 436, 807, doi: [10.1093/mnras/stt1617](https://doi.org/10.1093/mnras/stt1617)
- Barclay, T., Pepper, J., & Quintana, E. V. 2018, *ApJS*, 239, 2, doi: [10.3847/1538-4365/aae3e9](https://doi.org/10.3847/1538-4365/aae3e9)
- Borucki, W. J., Koch, D., Basri, G., et al. 2010, *Science*, 327, 977, doi: [10.1126/science.1185402](https://doi.org/10.1126/science.1185402)
- Box, G. E. P., Jenkins, G. M., Reinsel, G. C., & Ljung, G. M. 2015, 'Time Series Analysis: Forecasting and Control', '5th edition' edn. ("Wiley")
- Brown, T. M. 2003, *ApJL*, 593, L125, doi: [10.1086/378310](https://doi.org/10.1086/378310)
- Caceres, G. A., & Feigelson, E. D. 2022, TCF: Transit Comb Filter periodogram, *Astrophysics Source Code Library*, record ascl:2206.002. <http://ascl.net/2206.002>
- Caceres, G. A., Feigelson, E. D., Babu, G. J., et al. 2019a, *The Astronomical Journal*, 158, 57, doi: [10.3847/1538-3881/ab26b8](https://doi.org/10.3847/1538-3881/ab26b8)
- . 2019b, *The Astronomical Journal*, 158, 58, doi: [10.3847/1538-3881/ab26ba](https://doi.org/10.3847/1538-3881/ab26ba)
- Castillo, E., Hadi, A. S., Balakrishnan, N., & Sarabia, J.-M. 2004, *Extreme Value and Related Models with Applications in Engineering and Science* (Wiley Hoboken, NJ). "https://www.wiley.com/en-us/Extreme+Value+and+Related+Models+with+Applications+in+Engineering+and+Science-p-9780471671725"
- Coles, S., Bawa, J., Trenner, L., & Dorazio, P. 2001, *An Introduction to Statistical Modeling of Extreme Values*, *Springer Series in Statistics* (Springer). <https://books.google.co.in/books?id=2nugUEaKqFEC>
- Davis, O., Devriendt, J., Colombi, S., Silk, J., & Pichon, C. 2011, *Monthly Notices of the Royal Astronomical Society*, 413, 2087, doi: [10.1111/j.1365-2966.2011.18286.x](https://doi.org/10.1111/j.1365-2966.2011.18286.x)
- Delisle, J. B., Hara, N., & Ségransan, D. 2020, *A&A*, 635, A83, doi: [10.1051/0004-6361/201936905](https://doi.org/10.1051/0004-6361/201936905)
- Dressing, C. D., & Charbonneau, D. 2015, *ApJ*, 807, 45, doi: [10.1088/0004-637X/807/1/45](https://doi.org/10.1088/0004-637X/807/1/45)
- Dworetzky, M. M. 1983, *MNRAS*, 203, 917, doi: [10.1093/mnras/203.4.917](https://doi.org/10.1093/mnras/203.4.917)
- Feigelson, E. D., Babu, G. J., & Caceres, G. A. 2018, *Frontiers in Physics*, 6, doi: [10.3389/fphy.2018.00080](https://doi.org/10.3389/fphy.2018.00080)
- Feinstein, A. D., Montet, B. T., Foreman-Mackey, D., et al. 2019, *PASP*, 131, 094502, doi: [10.1088/1538-3873/ab291c](https://doi.org/10.1088/1538-3873/ab291c)
- Ferreira, A., & de Haan, L. 2015, *The Annals of Statistics*, 43, 276, doi: [10.1214/14-AOS1280](https://doi.org/10.1214/14-AOS1280)
- Fisher, R. A., & Tippett, L. H. C. 1928, *Mathematical Proceedings of the Cambridge Philosophical Society*, 24, 180–190, doi: [10.1017/S0305004100015681](https://doi.org/10.1017/S0305004100015681)
- Foreman-Mackey, D., Luger, R., Agol, E., et al. 2021, *The Journal of Open Source Software*, 6, 3285, doi: [10.21105/joss.03285](https://doi.org/10.21105/joss.03285)
- Frescura, F. A. M., Engelbrecht, C. A., & Frank, B. S. 2007, *arXiv e-prints*, arXiv:0706.2225, doi: [10.48550/arXiv.0706.2225](https://doi.org/10.48550/arXiv.0706.2225)
- Frescura, F. A. M., Engelbrecht, C. A., & Frank, B. S. 2008, *Monthly Notices of the Royal Astronomical Society*, 388, 1693, doi: [10.1111/j.1365-2966.2008.13499.x](https://doi.org/10.1111/j.1365-2966.2008.13499.x)

- Fressin, F., Torres, G., Charbonneau, D., et al. 2013, *ApJ*, 766, 81, doi: [10.1088/0004-637X/766/2/81](https://doi.org/10.1088/0004-637X/766/2/81)
- Giertych, N., Williams, J. P., & Haravu, P. 2022, ""
- Gilleland, E., & Katz, R. W. 2016, *Journal of Statistical Software*, 72, 1, doi: [10.18637/jss.v072.i08](https://doi.org/10.18637/jss.v072.i08)
- Gilliland, R. L., Chaplin, W. J., Dunham, E. W., et al. 2011, *ApJS*, 197, 6, doi: [10.1088/0067-0049/197/1/6](https://doi.org/10.1088/0067-0049/197/1/6)
- Gnedenko, B. 1943, *Annals of Mathematics*, 44, 423.  
<http://www.jstor.org/stable/1968974>
- Graham, M. J., Drake, A. J., Djorgovski, S. G., et al. 2013, *Monthly Notices of the Royal Astronomical Society*, 434, 3423, doi: [10.1093/mnras/stt1264](https://doi.org/10.1093/mnras/stt1264)
- Gregory, P. C., & Lored, T. J. 1992, *ApJ*, 398, 146, doi: [10.1086/171844](https://doi.org/10.1086/171844)
- Guerrero, N. M., Seager, S., Huang, C. X., et al. 2021, *ApJS*, 254, 39, doi: [10.3847/1538-4365/abefe1](https://doi.org/10.3847/1538-4365/abefe1)
- Hedges, C. 2021, *Research Notes of the American Astronomical Society*, 5, 262, doi: [10.3847/2515-5172/ac376a](https://doi.org/10.3847/2515-5172/ac376a)
- Hippke, M., & Heller, R. 2019, *A&A*, 623, A39, doi: [10.1051/0004-6361/201834672](https://doi.org/10.1051/0004-6361/201834672)
- Horne, J. H., & Baliunas, S. L. 1986, *The Astrophysical Journal*, 302, 757
- Horne, K. 2003, in *Astronomical Society of the Pacific Conference Series*, Vol. 294, *Scientific Frontiers in Research on Extrasolar Planets*, ed. D. Deming & S. Seager, 361–370, doi: [10.48550/arXiv.astro-ph/0301249](https://doi.org/10.48550/arXiv.astro-ph/0301249)
- Howell, S. B., Sobek, C., Haas, M., et al. 2014, *PASP*, 126, 398, doi: [10.1086/676406](https://doi.org/10.1086/676406)
- Hyndman, R., Athanasopoulos, & et al. 2023, in "forecast: Forecasting functions for time series and linear models. R package version 8.21.  
<https://pkg.robjhyndman.com/forecast>
- Hyndman, R. J., & Athanasopoulos, G. 2021, "Forecasting: Principles and Practice, 3rd edn. (").  
<https://otexts.com/fpp3/>
- Hyndman, R. J., & Khandakar, Y. 2008, *Journal of Statistical Software*, 26, 1, doi: [10.18637/jss.v027.i03](https://doi.org/10.18637/jss.v027.i03)
- Jenkins, J. M., Caldwell, D. A., & Borucki, W. J. 2002, *The Astrophysical Journal*, 564, 495, doi: [10.1086/324143](https://doi.org/10.1086/324143)
- Jenkinson, A. F. 1955, *Quarterly Journal of the Royal Meteorological Society*, 81, 158–171, doi: [10.1002/qj.49708134804](https://doi.org/10.1002/qj.49708134804)
- Karatzoglou, A., Smola, A., & Hornik, K. 2023, in "kernlab: Kernel-Based Machine Learning Lab. R package version 0.9-31". <https://CRAN.R-project.org/package=kernlab>
- Karatzoglou, A., Smola, A., Hornik, K., & Zeileis, A. 2004, *Journal of Statistical Software*, 11, 1, doi: [10.18637/jss.v011.i09](https://doi.org/10.18637/jss.v011.i09)
- Koen, C. 1990, *The Astrophysical Journal*, 348, 700
- Koen, C. 2010, *MNRAS*, 401, 586, doi: [10.1111/j.1365-2966.2009.15680.x](https://doi.org/10.1111/j.1365-2966.2009.15680.x)
- . 2015, *MNRAS*, 449, 1098, doi: [10.1093/mnras/stv288](https://doi.org/10.1093/mnras/stv288)
- . 2021, *AJ*, 161, 281, doi: [10.3847/1538-3881/abf64e](https://doi.org/10.3847/1538-3881/abf64e)
- Kovács, G., Zucker, S., & Mazeh, T. 2002, *A&A*, 391, 369, doi: [10.1051/0004-6361:20020802](https://doi.org/10.1051/0004-6361:20020802)
- . 2016, BLS: Box-fitting Least Squares, *Astrophysics Source Code Library*, record ascl:1607.008.  
<http://ascl.net/1607.008>
- Kunimoto, M., Winn, J., Ricker, G. R., & Vanderspek, R. K. 2022, *AJ*, 163, 290, doi: [10.3847/1538-3881/ac68e3](https://doi.org/10.3847/1538-3881/ac68e3)
- Leadbetter, M. R., & Rootzen, H. 1988, *The Annals of Probability*, 16, 431.  
<http://www.jstor.org/stable/2243819>
- Lightkurve Collaboration, Cardoso, J. V. d. M., Hedges, C., et al. 2018a, *Lightkurve: Kepler and TESS time series analysis in Python*, *Astrophysics Source Code Library*, record ascl:1812.013. <http://ascl.net/1812.013>
- Lightkurve Collaboration, Cardoso, J. V. d. M., Hedges, C., et al. 2018b, *Lightkurve: Kepler and TESS time series analysis in Python*, *Astrophysics Source Code Library*.  
<http://ascl.net/1812.013>
- Lund, M. B., Pepper, J., & Stassun, K. G. 2014, *The Astronomical Journal*, 149, 16, doi: [10.1088/0004-6256/149/1/16](https://doi.org/10.1088/0004-6256/149/1/16)
- Maxted, P. F. L., Anderson, D. R., Cameron, A. C., et al. 2011, *Publications of the Astronomical Society of the Pacific*, 123, 547, doi: [10.1086/660007](https://doi.org/10.1086/660007)
- McQuillan, A., Mazeh, T., & Aigrain, S. 2014, *ApJS*, 211, 24, doi: [10.1088/0067-0049/211/2/24](https://doi.org/10.1088/0067-0049/211/2/24)
- Melton, E. J., Feigelson, E. D., Montalto, M., et al. 2023a, *arXiv e-prints*, arXiv:2302.06724, doi: [10.48550/arXiv.2302.06724](https://doi.org/10.48550/arXiv.2302.06724)
- . 2023b, *arXiv e-prints*, arXiv:2302.06700, doi: [10.48550/arXiv.2302.06700](https://doi.org/10.48550/arXiv.2302.06700)
- . 2023c, *arXiv e-prints*, arXiv:2302.06744, doi: [10.48550/arXiv.2302.06744](https://doi.org/10.48550/arXiv.2302.06744)
- Mersmann, O. 2021, *microbenchmark: Accurate Timing Functions*.  
<https://CRAN.R-project.org/package=microbenchmark>
- Montalto, M., Borsato, L., Granata, V., et al. 2020, *MNRAS*, 498, 1726, doi: [10.1093/mnras/staa2438](https://doi.org/10.1093/mnras/staa2438)
- NASA Exoplanet Science Institute. 2020, *Planetary Systems Table*, IPAC, doi: [10.26133/NEA12](https://doi.org/10.26133/NEA12)
- Ng, 1996, "Computational Statistics & Data Analysis", 22, 99, doi: [10.1016/0167-9473\(95\)00044-5](https://doi.org/10.1016/0167-9473(95)00044-5)
- Ng, P., & Maechler, M. 2007, "Statistical Modelling", 7, 315, doi: [10.1177/1471082X0700700403](https://doi.org/10.1177/1471082X0700700403)

- Ng, P. T., & Maechler, M. 2022, in COBS – Constrained B-splines (Sparse matrix based). R package version 1.3-5. <https://CRAN.R-project.org/package=cobs>
- Ofir, A. 2014, *A&A*, 561, A138, doi: [10.1051/0004-6361/201220860](https://doi.org/10.1051/0004-6361/201220860)
- Panahi, A., & Zucker, S. 2021, *PASP*, 133, 024502, doi: [10.1088/1538-3873/abd9ab](https://doi.org/10.1088/1538-3873/abd9ab)
- Percival, D. B., & Walden, A. T. 2009, "Spectral Analysis for Univariate Time Series", 2nd edn. (Cambridge University Press)
- Pont, F., Zucker, S., & Queloz, D. 2006, *MNRAS*, 373, 231, doi: [10.1111/j.1365-2966.2006.11012.x](https://doi.org/10.1111/j.1365-2966.2006.11012.x)
- Pratt, J., Baraffe, I., Goffrey, T., et al. 2017, *A&A*, 604, A125, doi: [10.1051/0004-6361/201630362](https://doi.org/10.1051/0004-6361/201630362)
- R Core Team. 2022, R: A Language and Environment for Statistical Computing, R Foundation for Statistical Computing, Vienna, Austria. <https://www.R-project.org/>
- Rauer, H., Catala, C., Aerts, C., et al. 2014, *Experimental Astronomy*, 38, 249, doi: [10.1007/s10686-014-9383-4](https://doi.org/10.1007/s10686-014-9383-4)
- Ricker, G. R., Winn, J. N., Vanderspek, R., et al. 2015, *Journal of Astronomical Telescopes, Instruments, and Systems*, 1, 014003, doi: [10.1117/1.JATIS.1.1.014003](https://doi.org/10.1117/1.JATIS.1.1.014003)
- Scargle, J. D. 1982, *The Astrophysical Journal*, 263, 835
- Scargle, J. D. 1989, *ApJ*, 343, 874, doi: [10.1086/167757](https://doi.org/10.1086/167757)
- Shahaf, S., Zackay, B., Mazeh, T., Faigler, S., & Ivashtenko, O. 2022, *Monthly Notices of the Royal Astronomical Society*, 513, 2732, doi: [10.1093/mnras/stac960](https://doi.org/10.1093/mnras/stac960)
- Shallue, C. J., & Vanderburg, A. 2018, *The Astronomical Journal*, 155, 94, doi: [10.3847/1538-3881/aa9e09](https://doi.org/10.3847/1538-3881/aa9e09)
- Spergel, D., Gehrels, N., Baltay, C., et al. 2015, arXiv e-prints, arXiv:1503.03757, doi: [10.48550/arXiv.1503.03757](https://doi.org/10.48550/arXiv.1503.03757)
- Stellingwerf, R. F. 1978, *ApJ*, 224, 953, doi: [10.1086/156444](https://doi.org/10.1086/156444)
- Stephens, M. A. 1974, *Journal of the American Statistical Association*, 69, 730. <http://www.jstor.org/stable/2286009>
- Sulis, S., Mary, D., & Bigot, L. 2017, *IEEE Transactions on Signal Processing*, 65, 2136, doi: [10.1109/TSP.2017.2652391](https://doi.org/10.1109/TSP.2017.2652391)
- Suveges, M. 2012, in *Seventh Conference on Astronomical Data Analysis*, ed. J.-L. Starck & C. Surace, 16
- Süveges, M. 2014, *Monthly Notices of the Royal Astronomical Society*, 440, 2099, doi: [10.1093/mnras/stu372](https://doi.org/10.1093/mnras/stu372)
- Süveges, M., Guy, L. P., Eyer, L., et al. 2015, *Monthly Notices of the Royal Astronomical Society*, 450, 2052, doi: [10.1093/mnras/stv719](https://doi.org/10.1093/mnras/stv719)
- Thompson, S. E., Mullally, F., Coughlin, J., et al. 2015, *ApJ*, 812, 46, doi: [10.1088/0004-637X/812/1/46](https://doi.org/10.1088/0004-637X/812/1/46)
- Torres, G., Fressin, F., Batalha, N. M., et al. 2011, *ApJ*, 727, 24, doi: [10.1088/0004-637X/727/1/24](https://doi.org/10.1088/0004-637X/727/1/24)
- Twicken, J. D., Jenkins, J. M., Seader, S. E., et al. 2016, *AJ*, 152, 158, doi: [10.3847/0004-6256/152/6/158](https://doi.org/10.3847/0004-6256/152/6/158)
- Twicken, J. D., Catanzarite, J. H., Clarke, B. D., et al. 2018, *PASP*, 130, 064502, doi: [10.1088/1538-3873/aab694](https://doi.org/10.1088/1538-3873/aab694)
- Vanderburg, A., & Johnson, J. A. 2014, *PASP*, 126, 948, doi: [10.1086/678764](https://doi.org/10.1086/678764)
- Vanderburg, A., Latham, D. W., Buchhave, L. A., et al. 2016, *ApJS*, 222, 14, doi: [10.3847/0067-0049/222/1/14](https://doi.org/10.3847/0067-0049/222/1/14)
- Vanderburg, A., Latham, D. W., Buchhave, L. A., et al. 2016, *The Astrophysical Journal Supplement Series*, 222, 14, doi: [10.3847/0067-0049/222/1/14](https://doi.org/10.3847/0067-0049/222/1/14)
- VanderPlas, J. T. 2018, *ApJS*, 236, 16, doi: [10.3847/1538-4365/aab766](https://doi.org/10.3847/1538-4365/aab766)
- Vio, R., Andreani, P., Biggs, A., & Hayatsu, N. 2019, *A&A*, 627, A103, doi: [10.1051/0004-6361/201834854](https://doi.org/10.1051/0004-6361/201834854)
- Waizmann, J.-C., Ettore, S., & Moscardini, L. 2012, *Monthly Notices of the Royal Astronomical Society*, 420, 1754, doi: [10.1111/j.1365-2966.2011.20171.x](https://doi.org/10.1111/j.1365-2966.2011.20171.x)
- Waldmann, I. P. 2012, *ApJ*, 747, 12, doi: [10.1088/0004-637X/747/1/12](https://doi.org/10.1088/0004-637X/747/1/12)
- Williams, C. K. I., & Barber, D. 1998, *IEEE Transactions on Pattern Analysis and Machine Intelligence*, 20, 1342
- Zucker, S. 2015, *MNRAS*, 449, 2723, doi: [10.1093/mnras/stv509](https://doi.org/10.1093/mnras/stv509)